POLITECNICO DI TORINO
Repository ISTITUZIONALE

Turbulence distortion and leading-edge noise

Terms of use:

Publisher copyright

(Article begins on next page)

09 March 2025

Turbulence distortion and leading-edge noise

A. Piccolo ✉ (ID) ; R. Zamponi (ID) ; F. Avallone (ID) ; D. Ragni (ID)

Check for updates

View Online   Export Citation

Articles You May Be Interested In

Numerical study of inflow turbulence distortion and noise for airfoils

Physics of Fluids (November 2023)

Aeroacoustic design and broadband noise predictions of a fan stage with serrated outlet guide vanes

Physics of Fluids (October 2020)

Fast and accurate analytical modeling of broadband noise for a low-speed fan

J. Acoust. Soc. Am. (May 2018)

23 January 2025 12:30:40

AIP Publishing

Physics of Fluids

Special Topics Open for Submissions

Learn More

AIP Publishing

Turbulence distortion and leading-edge noise

View Online   Export Citation   CrossMark

A. Piccolo,[1,a)] (ID)   R. Zamponi,[1,2] (ID)   F. Avallone,[3] (ID)   and D. Ragni[1] (ID)

AFFILIATIONS

[1]Delft University of Technology, Kluyverweg 1, 2629 HS Delft, The Netherlands
[2]von Kármán Institute for Fluid Dynamics, Waterloosest. 72, B-1640 Sint-Genesius-Rode, Belgium
[3]Politecnico di Torino, Corso Duca degli Abruzzi 24, 10129 Torino, Italy

[a)]Author to whom correspondence should be addressed: a.piccolo@tudelft.nl

ABSTRACT

The distortion of turbulence interacting with thick airfoils is analyzed with scale-resolved numerical simulations to elucidate its impact on leading-edge-noise generation and prediction. The effect of the leading-edge geometry is investigated by considering two airfoils with different leading-edge radii subjected to grid-generated turbulence. The velocity field is shown to be altered near the stagnation point, in a region whose extension does not depend on the leading-edge radius. Here, the deformation of large-scale turbulence causes the amplitude of the upwash velocity fluctuations to increase in the low-frequency range of the spectrum because of the blockage exerted by the surface. Conversely, the distortion of small-scale structures leads to an exponential decay of the spectrum at high frequencies due to the alteration of the vorticity field. The prevalence of a distortion mechanism over the other is found to depend on the size of the turbulent structures with respect to the curvilinear length from the stagnation point to the location where surface-pressure fluctuations and pressure gradient peak. This occurs at the curvilinear abscissa where the curvature changes the most. The same high-frequency exponential-decay slope observed for the upwash velocity is retrieved for surface-pressure spectra in the leading-edge region, suggesting that the airfoil unsteady response is induced by the distorted velocity field. This physical mechanism can be accounted for in Amiet's model by using a distorted turbulence spectrum as input and accounting for the increased amplitude of the distorted gust in the aeroacoustic transfer function, retrieving an accurate noise prediction for both airfoils.

I. INTRODUCTION

Leading-edge noise, also known as inflow-turbulence noise, is a flow-induced sound source produced by the interaction of incoming turbulence with an aerodynamic surface. Identified as a sound-generation mechanism and modeled analytically since the seventies,[1–5] several reasons justify the long-lasting interest in academic and industrial research for the analysis of this noise source: the complexity of the physics involved in the sound production, the successful results achieved in the reduction of other prevailing noise sources,[6,7] and its relevance in high-speed applications, e.g., propellers and rotors in propulsive systems,[5,8,9] as well as low-speed ones, e.g., fans in cooling systems or wind turbines.[10–12] In all these sectors, the design and optimization phases depend on the accuracy of the noise prediction provided by low-fidelity methods to minimize the computational cost.

The first approach to predict leading-edge noise was proposed by Amiet.[2] In this semi-analytical method, the power spectral density (PSD) of the far-field noise produced by a flat plate in a subsonic turbulent flow is related to the characteristics of the upstream turbulence by means of a transfer function that models the surface response to a sinusoidal gust. The agreement with the experimental data was shown to be satisfactory for flat plates and thin airfoils, in particular for high-speed flow.[3,13] Nevertheless, the accuracy of the method decreases in the case of thicker aerodynamic surfaces, in particular in the high-frequency range, as pointed out by Paterson and Amiet.[3] Such a discrepancy was attributed to the fact that the model does not take into account effects due to the real geometry of the blade. The breakdown of the theory was observed to occur for Strouhal numbers $ft/U_\infty \geq 1$, with f being the sound frequency, t the thickness of the body, and U_∞ the free-stream velocity, i.e., for wavelengths of the incoming turbulent structures smaller than the thickness of the airfoil. Indeed, the deformation undergone by these structures during the interaction with a thick leading edge is not taken into account in the model, which adopts as input a canonical turbulence spectrum, such as the von Kármán or the Liepmann ones.

The effects of the airfoil geometry on its aerodynamic and acoustic response in the presence of incoming turbulence were confirmed by

23 January 2025 12:30:40

the analytical study of Goldstein and Atassi,[14] which was based on the distortion of a gust, described as a small vortical disturbance, convected by the mean flow. The model showed that the influence of the airfoil thickness on the streamlines could lead to an additional deformation of the incoming gusts, causing a variation of the unsteady lift in the high-frequency range. A following experimental investigation of Olsen and Wagner[15] corroborated this result from an acoustic point of view by reporting a far-field noise attenuation in the high-frequency range as the thickness increases. Atassi *et al.*[16] and Lockard and Morris[17] extended these findings by noticing that the effects of thickness occurred for gust wavelengths shorter than the airfoil chord and mostly for downstream observer locations. Glegg and Devenport[18] showed that, for blade-vortex interaction, the peak of unsteady lift on the leading edge due to vortex is reduced when the vortical element is closer to the surface. Moreover, as the airfoil thickness increases, the peak diminishes further and moves downstream. In subsequent work, Glegg and Devenport[19] employed a panel method to develop a noise-prediction model able to capture this high-frequency attenuation due to the thickness, improving the prediction of Amiet's model.

Further investigations have been conducted to determine how the geometrical characteristics of the airfoil impact the distortion of incoming turbulent eddies and far-field noise. Oerlemans[20] found that the shape of the leading edge, more precisely its *sharpness*, could affect noise-generation efficiency, with more rounded airfoils producing less noise. The same direction was taken by Hall *et al.*,[21] who intervened on the leading-edge shape by modifying the first 10% of an *ad hoc* designed airfoil, observing that the maximum noise reduction was obtained for reduced frequencies, computed with respect to the leading-edge thickness, on the order of 1. It was hypothesized that the changes in the flow incidence affected the noise generation, thus highlighting the relevance of the pressure distribution over the airfoil on far-field noise and excluding a unique dependence on the relation between the incoming turbulence scale and the leading-edge thickness. The effects of turbulence distortion on noise generation and the role of airfoil geometry were widely investigated by Chaitanya *et al.*,[22] who concluded that the airfoil thickness and leading-edge shape are the main geometrical characteristics affecting the noise-generation efficiency, with the latter being particularly relevant in the high-frequency range. No significant effect of camber and angle of attack was found in the case of isotropic turbulence interacting with the airfoil, as also confirmed by Devenport *et al.*[23] Gill *et al.*[24] conducted a systematic study to investigate the role of airfoil thickness and leading-edge radius in high-frequency noise attenuation. The analysis was carried out using single-frequency harmonic gusts interacting with several NACA 4-digit airfoils. Interestingly, the noise mitigation obtained by increasing the leading-edge radius was shown to be smaller and occurred at higher frequencies than that obtained for larger thicknesses. In addition, the noise reduction associated with thicker airfoils was more evident for downstream observer positions, while an increase was found in upstream positions in the case of larger leading-edge radii. The authors attributed these effects to the distortion of the vortical gusts due to the velocity gradients present in the stagnation region, which caused the gust wavefront to be smoothed and its amplitude to decrease. Bowen *et al.*[25] assessed the influence of the turbulence characteristics on the leading-edge noise with the purpose of investigating the alteration of the velocity field and the surface-pressure distribution in the stagnation region of an airfoil. The sound-production efficiency

was shown to be directly related to the intensity and to the integral length scale of the incoming turbulence, which also affects the energy levels of the surface-pressure spectra on the leading edge. At the same time, it was concluded that the noise generation at the leading edge was mainly induced by the flow field in the vicinity of the stagnation point.

Several approaches have been developed to enhance the accuracy of leading-edge noise prediction by taking into account airfoil thickness effects. An analytical procedure was followed by Guidati *et al.*,[26] who employed a boundary-element method to model the sound generated by point vortices convected along the mean-flow streamlines to formulate a correction to Amiet's model. Subsequently, Moriarty *et al.*[13] showed that such a combination was able to provide a satisfying agreement with the experimental data in terms of the spectrum decay slope at different angles of attack and Mach numbers, but a tuning constant of 10 dB had to be added to the prediction. Moreover, a significant underestimation was still observed in the high-frequency range in comparison to the measurements for thicker airfoils. Gershfeld[27] obtained a good agreement with the experimental measurements of Paterson and Amiet[3] by implementing an exponential function to model the effects of airfoil thickness on noise radiation. The correction was based on a rigid surface Green's function taking into account airfoil thickness and the back-scattering due to the airfoil non-compactness.[28] Also, Lysak *et al.*[29] and Kim *et al.*[30] observed the airfoil thickness to cause an exponential decay in the high-frequency range for the unsteady response of the blade and the far-field noise, respectively. In both their works, a correction factor to flat-plate-based noise-prediction models was developed in the form of an exponential function of the Mach number, airfoil thickness, and leading-edge thickness by fitting the respective reference data, with whom a good agreement was shown.

Recent efforts have focused on describing the alteration of the turbulent flow field in the interaction with the airfoil to improve low-fidelity noise-prediction methods. The results of the rapid distortion theory (RDT) of Hunt,[31] which models turbulence interaction with bluff bodies, were employed to account for turbulence-distortion effects. Hunt's formulation built on the works of Ribner and Tucker[32] and Batchelor and Proudman,[33] extending the analyses of Prandtl[34] and Taylor[35] on vorticity-field distortion in the contraction section of a wind tunnel. The RDT computes the distortion of initially homogeneous turbulence around a circular cylinder by means of a wavenumber analysis. Velocity spectra and variances were derived in the asymptotic cases where the turbulence integral length scale L_x is much smaller or larger than the characteristic dimension of the body a, e.g., the radius in the case of the cylinder. The ratio L_x/a between these two parameters was shown to determine the different mechanisms by which turbulent structures are deformed. In the case $L_x/a \gg 1$, the prevailing distortion mechanism is due to the blockage caused by the body. This causes a momentum transfer between the streamwise and upwash velocity components of a fluid element approaching the cylinder stagnation point: the streamwise velocity fluctuations decrease while the upwash ones increase. For small-scale structures ($L_x/a \ll 1$) or high wavenumbers of the incident turbulence, the vorticity-field deformation due to the deflection of the streamlines dominates the distortion mechanism. As vortex lines are convected toward the surface, they stretch or shorten, causing the streamwise and spanwise velocity fluctuations to increase and the upwash ones to decrease.

The work of Mish and Devenport[36,37] proved that, in the vicinity of the stagnation point, the distortion of the turbulence structures interacting with an airfoil is comparable to that occurring for a circular cylinder with the same radius as the leading-edge circle. This outcome allowed the extension of the findings of the RDT from the case of the cylinder to more relevant applications in the aeroacoustic field, as in the case of realistic airfoil geometries. Moreau and Roger[38] proposed a modification of the analytical expression of the canonical turbulence spectrum used as input into Amiet's model to account for the distortion of small-scale structures caused by the presence of the body: a correction of the slope of the von Kármán spectrum in the high-frequency range from $-5/3$ to $-10/3$, based on the findings of the RDT, was introduced. A good agreement was achieved with experimental measurements in terms of the high-frequency decay slope of the far-field noise spectrum and noise levels, but, as specified by the authors, the validity of the correction was limited to the particular case in analysis and could not be generalized if the characteristics of the distorted turbulence were not properly modeled. Similar approaches adopted by Christophe[39] and De Santana et al.[40] confirmed that the distortion of the turbulent structures occurring in the vicinity of the leading edge of non-thin airfoils could play a role in the noise generation and, hence, could affect noise prediction. This line of research was continued by dos Santos et al.,[41] who proposed an empirical correction to better predict turbulence spectra in the dissipation range through a modified von Kármán expression. The corrected turbulence spectrum was then used as input in Amiet's model to improve the prediction accuracy in the high-frequency range.[42] Nevertheless, the reliability of the method to predict leading-edge noise depends on the identification of a representative position in the flow field where the integral length scale and turbulence intensity, which are needed to scale the corrected analytical von Kármán expression, shall be sampled. An alternative approach was proposed by Piccolo et al.,[43] who applied Amiet's model with a turbulence spectrum directly sampled in the vicinity of the stagnation point, more precisely at the position along the airfoil surface where the root mean square of the pressure fluctuation is maximum, in the case of rod-generated turbulence interacting with a NACA 0012. This procedure yielded a noise prediction in good agreement with the results obtained with the Ffowcs-Williams and Hawkings (FWH) analogy,[44] both in terms of sound pressure level (SPL) and directivity patterns, in the particular case of large-scale turbulence characterized by a tonal component.

All the body of work mentioned above has shown that the distortion of turbulent structures in the interaction with a solid body can significantly affect leading-edge noise generation and that low-fidelity methods can benefit from the modeling of these effects. However, most of the corrective methods currently available in the literature, despite identifying the use of RDT results as a valid approach to enhance Amiet's model accuracy, are limited by the lack of a thorough physical investigation to support them. As a consequence, the proposed methodologies are hardly generalizable and rely on the empirical tuning of the input parameters and the choice of a sampling location to evaluate turbulence characteristics.

Therefore, the present study intends to improve the understanding of turbulence-distortion mechanisms and their impact on sound radiation by analyzing the velocity field and unsteady surface pressures in the stagnation region of realistic airfoils. This physical description represents a key step for the future development of semi-analytical

corrections enhancing low-fidelity methods by employing distorted-turbulence inputs and calculating them from upstream conditions. Indeed, the results discussed in the paper indicate that turbulence-distortion effects, both on the velocity spectrum and the acoustic response, should be estimated as close as possible to the stagnation point to achieve accurate modeling of the impact on noise generation. For this purpose, a numerical set-up has been developed reproducing the experimental one at the University of Southampton.[22] The Lattice-Boltzmann method (LBM) based software PowerFLOW has been used to study grid-generated turbulence interacting with two different airfoils, i.e., a standard NACA 0012 and a NACA 0012-103, the latter belonging to the NACA modified 4-digit series. This second airfoil has been considered to investigate the effect of different leading-edge shapes while keeping the same thickness.

The outline of the paper is the following. In Sec. II, information regarding the flow solver and the numerical set-ups are reported. The validation of the numerical simulations is shown in Sec. III, while the analyses of the flow field for the two configurations and the noise prediction computed with a modified implementation of Amiet's model are presented in Sec. IV. Finally, the conclusions are drawn in Sec. V.

II. METHODOLOGY

A. Flow solver

The commercial software Simulia PowerFLOW 6-2021 is used to compute the flow field. The software is based on the LBM, which models the motion and the collisions of fluid particles at mesoscopic scales through particle-distribution functions. Local integration of these functions, aligned with a finite number of predefined directions, allows the calculation of flow density, momentum, and internal energy.[45] The Boltzmann equation is solved on a Cartesian mesh (lattice), with the discretization performed through 19 discrete velocity vectors in three dimensions, i.e., D3Q19, using a third-order truncation of the Chapman–Enskog expansion. This scheme has been shown to be accurate for approximating the Navier–Stokes equation in the case of a perfect gas at low Mach numbers and isothermal conditions.[46] The discretized form of the equation reads

$$F_i(\boldsymbol{x} + \boldsymbol{V}_n \Delta t, t + \Delta t) - F_i(\boldsymbol{x}, t) = C_i(\boldsymbol{x}, t), \tag{1}$$

where F_i and $\boldsymbol{V}_i$ are the particle distribution function and the discrete particle velocity along the ith lattice direction at position x and time instant t, respectively.

The collision term C_i is based on the Bhatnagar–Gross–Krook (BGK) model.[47] Despite its limitations[48,49] and the development of various improvements,[50,51] this model remains widely used for its simplicity and computational efficiency.[52,53] The BGK model indeed simplifies the discrete LB equation by replacing the collision operator with a single relaxation time τ. The model considers that, within this timescale, the local distribution function approaches the equilibrium one F_i^{eq}, which is approximated with a second-order expansion.[46] This means that the same rate is assumed for all the scales of the relaxation processes, rather than being a function of F_i.

The numerical solver uses a very-large-eddy simulation (VLES) model to account for unresolved scales of turbulence. A modified two-equation $k - \epsilon$ renormalization group (RNG) turbulence model is used to calculate the turbulent relaxation time which is added to the viscous relaxation time[54]

$$\tau_{\mathrm{eff}} = \tau + C_\mu \frac{k^2/\epsilon}{(1+\eta^2)^{1/2}}, \qquad (2)$$

where $C_\mu = 0.09$, and η combines local strain, vorticity, and helicity parameters.[55] This mitigates subgrid-scale viscosity so that the resolved large-scale structures are not numerically damped. This relaxation time then calibrates the Boltzmann model to the characteristic time scales of a turbulent flow motion. Reynolds stresses are, hence, an inherent consequence of the chaotic exchange of momentum driven by the turbulent flow. The non-linearity of the stresses is correctly captured by the Chapman–Enskog expansion, making the model suited to represent turbulence in a state far from equilibrium.[56]

The LB scheme is solved on a three-dimensional lattice whose basic element is the voxel, i.e., volumetric pixel, whose size varies by a factor 2 in adjacent resolution regions. Surface elements discretize solid surfaces where they intersect voxels. Fluid-particle interaction with the solid surface is governed by wall-boundary conditions, such as a particle bounce-back process for no-slip walls and a specular reflection for slip walls.[57] The wall-shear stress is approximated by means of a wall function applied on the first wall-adjacent voxel. This function is based on the generalized law-of-the-wall model,[58] extended to consider the effects of pressure gradient and surface roughness.

The FWH analogy, in formulation 1A of Farassat and Succi[59] extended to a convective wave equation,[60] is used in the present work to calculate far-field noise. The formulation is implemented in the time domain using a source-time-dominant algorithm.[61] The analogy has been applied by sampling pressure fluctuations on the airfoil surface, making it possible to consider a distribution of acoustic dipoles and monopoles on the surface[62] and to neglect other non-linear contributions, i.e., quadrupole sources.

B. Simulation set-up

The selected test case reproduces the experimental set-up of the open-jet wind tunnel facility at the Institute of Sound and Vibration Research (ISVR) at the University of Southampton. A sketch of the numerical set-up is reported in Fig. 1. The experimental campaign conducted by Chaitanya *et al.*[22] is considered as a reference.

The airfoils investigated are a NACA 0012 and a NACA 0012-103 with a chord of $c = 0.15$ m and a span of $L = 0.45$ m. The airfoil is placed at a zero angle of attack at the center of the simulation domain, whose dimensions are $5 \times 5 \times 5$ m^3. The reference system is defined with x as the streamwise direction, along which the velocity component is u, y as the upwash direction with v as the velocity component, and z as the spanwise direction with velocity component w. A rectangular convergent nozzle of length 1.35 m is positioned 1 chord upstream of the leading edge of the airfoil. The exit section of the nozzle is 0.45 m wide and 0.15 m high, while the inlet section is a square of side 1.3 m. Upstream of the inlet section, a rectangular duct is added to assign the inlet boundary condition on the domain boundary, while two side-plates, with a height equal to 0.225 m and length equal to 0.375 m, have been placed at the nozzle exit section to the sides of the airfoil. A rectangular grid, used to generate turbulence and shown in the detail of Fig. 1, is placed inside the nozzle 0.63 m upstream of the nozzle exit. The grid is made of square rods that are 0.012 m thick, while the distance between the rods is 0.034 m, meaning that the
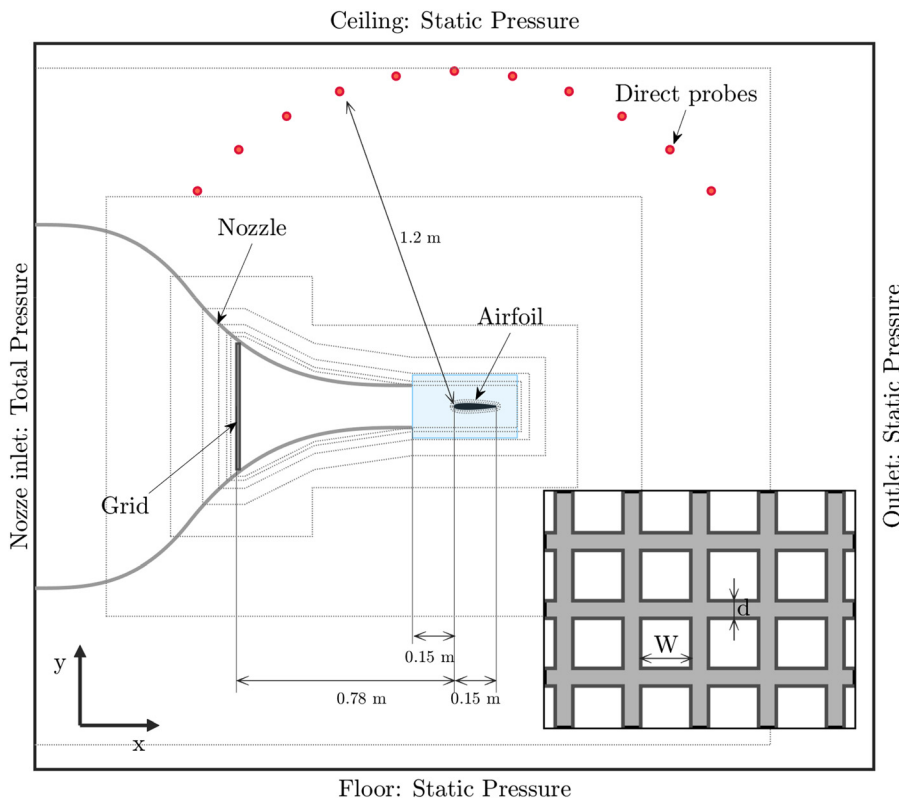

FIG. 1. Sketch of the simulation domain. The size of the volume is not drawn to scale. The resolution regions are qualitatively represented using dotted lines. The detail in the bottom right corner depicts a sketch of the turbulence-generating grid placed inside the nozzle. The thickness of the square bars d is equal to 0.012 m and the width W of the gap is 0.034 m.

TABLE I. Geometrical information about the rectangular grid.

Width (m)	Height (m)	Gap, W (m)	Rod thickness, d (m)	Pattern period, W + d (m)	Solidity, σ_{grid} (%)
0.46	0.61	0.034	0.012	0.046	55

period of the pattern is 0.046 m. The overall dimension of the grid is 0.46×0.61 m². All the geometrical information regarding the grid is reported in Table I.

The free-stream velocity is set equal to 60 m s^{-1} (corresponding to a Reynolds number calculated with respect to the chord equal to $Re = 6.2 \times 10^5$) at $x/c = -0.033$ upstream of the position of the leading edge in the configuration without the airfoil. This is obtained by imposing total pressure at the nozzle inlet and accounting for the head loss through the rectangular grid, calculated using the following expression from Roach[63]

$$\frac{\Delta p}{q_\infty} = A \left(\frac{1}{\beta_{grid}^2} - 1 \right)^B,$$

where the Δp across the rectangular grid, non-dimensionalized with respect to the upstream dynamic pressure q, is expressed as a function of the grid porosity β_{grid} and the coefficients A and B, which are a function of the Reynolds number, Mach number, and grid geometry. For the present case, they have been set equal to 0.98 and 1.09, respectively. The friction loss along the nozzle is neglected since the walls are set as frictionless walls. A static pressure equal to 101 325 Pa is set on the other boundaries of the simulation domain, i.e., the inlet around the nozzle inlet section, the outlet, the ceiling, the floor, and the two lateral sides of the volume.

In the finest resolution configuration, the simulation volume is subdivided into 10 refinement regions. As observed in Fig. 1, the resolution is kept constant from the grid to the airfoil to avoid numerical effects on turbulence convection. Two offsets placed around the airfoil allow a further decrease in the voxel size, reaching a value of 1.79 $\times 10^{-4}$ m next to the airfoil surface for the finest grid investigated. An average $y^+ = 19$ is, hence, achieved along the body. The domain for the finest resolution configuration is discretized with 660×10^6 voxels.

For the finest resolution, a physical time step of 3.046×10^{-7} s is employed to carry out the simulation, whose overall duration is 0.167 s. This is set in order to have 10 repetitions of the cycle at the lowest frequency considered (60 Hz). Taking into account the free-stream velocity and the airfoil chord, the duration of the simulation corresponds to 67 flow passes. Data have been saved after a transient of 25 flow passes (0.0625 s), defined by monitoring the convergence of the total pressure at the nozzle inlet.

Far-field noise is obtained through Ffowcs-Williams and Hawking's analogy using the pressure acquired on the airfoil surface. Data have been saved on the body at a rate of 30 kHz. The same frequency is used to sample quantities in the flow field in the vicinity of the airfoil. All the PSDs are one-sided and have been calculated using Welch's method with a Hanning window characterized by 50% overlap to obtain a 100 Hz frequency resolution. Eleven direct probes, shown in Fig. 1 as red dots, have been placed along an arc of radius R = 1.2 m between $\theta = 2\pi/9$ and $\theta = 7\pi/9$ measured from the downstream direction in the midspan plane of the airfoil and centered at the leading edge with an angular separation of $\Delta\theta = \pi/18$.

The two airfoils under analysis are shown in Fig. 2. The first airfoil is a standard NACA 0012, while the second one is a NACA 0012-103, belonging to the NACA-modified 4-digit series.[22,24,64] Following the notation used for this series, a standard NACA 0012 would be indicated as NACA 0012-63, where 6 is the value of a parameter r_{idx} related to the length of the leading-edge radius through the relation

$$r_{LE} = 1.1019 \left(\frac{t r_{idx}}{6} \right)^2 c,$$

with t being the thickness of the airfoil. The second digit of the numerical appendix indicates the position of maximum thickness. As a consequence, NACA 0012-103 will have an increased radius of the leading edge, being $r_{idx} = 10$, but the same thickness and same position of maximum thickness of the other airfoil investigated. The radius of the leading edge for the standard NACA 0012 is $r_{LE,0012} = 2.4 \times 10^{-3}$ m, while for NACA 0012-103 is $r_{LE,0012-103} = 6.6 \times 10^{-3}$ m. The geometrical data are reported in Table II. These two airfoils have been selected to analyze the contribution of a different curvature distribution on the leading-edge noise generation and turbulence distortion, keeping the same airfoil thickness.

The curvature of the airfoil is calculated analytically starting from the formulation of the NACA airfoils using the following expression

$$\kappa_s = \frac{\ddot{y}}{\left(1 + \dot{y}^2\right)^{3/2}},$$

where y represents the ordinate of the curve representing the NACA airfoil, and the derivation, indicated with the dot, is performed with respect to the independent coordinate x. Taking into account that the curvature can be expressed as the inverse of the radius of curvature, κ_s is non-dimensionalized by multiplying it by the radius of the airfoil leading edge. The non-dimensionalized curvature is indicated with C_s.
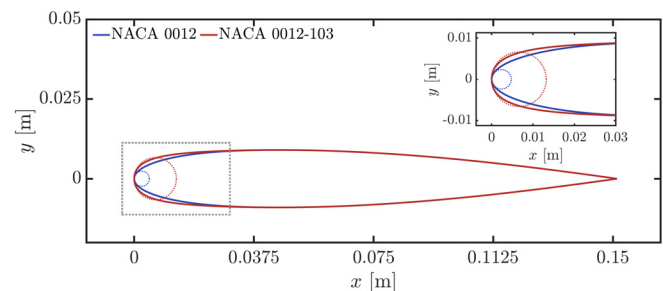

FIG. 2. Airfoils analyzed in the present work. A standard NACA 0012 is compared to a NACA 0012-103, part of the modified 4-digit series, which differs only for the radius of the leading edge.

TABLE II. Geometrical information of the two investigated airfoils.

	Chord, c (m)	Span, L (m)	Thickness, t (m)	LE radius, r_{LE} (m)
NACA 0012	0.15	0.45	0.018	2.4×10^{-3}
NACA 0012-103	0.15	0.45	0.018	6.6×10^{-3}

III. GRID-INDEPENDENCE STUDY AND VALIDATION

A. Grid-independence study

The grid-independence study was performed for the NACA-0012 case. For this configuration, five simulations with different resolutions have been carried out. With respect to the coarsest simulation, identified as "resolution level 1," the following one, i.e., "resolution level 2," is obtained using a refinement factor of 2. The third and the fourth levels of refinement have been achieved by refining the second resolution level with factors of 1.5 and 2, respectively. The fifth and finest resolution level is obtained by adding a further refinement region on the airfoil surface. Convergence is assessed in terms of sound power level (PWL) and time-averaged lift and drag coefficients of the airfoil, i.e., $\overline{C}_L$ and $\overline{C}_D$, respectively. Table III reports additional information about the different resolution levels.

The solid formulation of the FWH analogy is employed to calculate the far-field noise at the virtual microphones described in Sec. II B. The PWL is computed with the expression used in the reference experimental campaign

$$\text{PWL} = \left(\frac{\text{LR}}{\rho_\infty c_\infty}\right)\left[\sum_{i=1}^{N-1}\frac{S_{pp}(f,\theta_i)+S_{pp}(f,\theta_{i+1})}{2}\Delta\theta\right], \quad (3)$$

with L being the span of the airfoil, R the radius of the microphone array, c_∞ the speed of sound, and ρ_∞ the density of air. $S_{pp}(f,\theta_i)$ is the power spectral density of the far-field acoustic pressure at the position θ_i, while $\Delta\theta$ is the angular separation between two adjacent microphones. The procedure is explained in further detail by Narayanan et al.[65] This same expression has been used to calculate the PWL also in Secs. III B and IV.

The comparison of the PWLs for the different resolution levels is illustrated in Fig. 3 as a function of St_t, computed with respect to the airfoil thickness. The Strouhal range from $St_t = 0.15$ to 1.5 is highlighted since leading-edge noise dominates in this range.[22] The transparent gray patches in the plots cover the frequency ranges where background noise ($St_t < 0.15$) and self-noise ($St_t < 1.5$) prevail in the
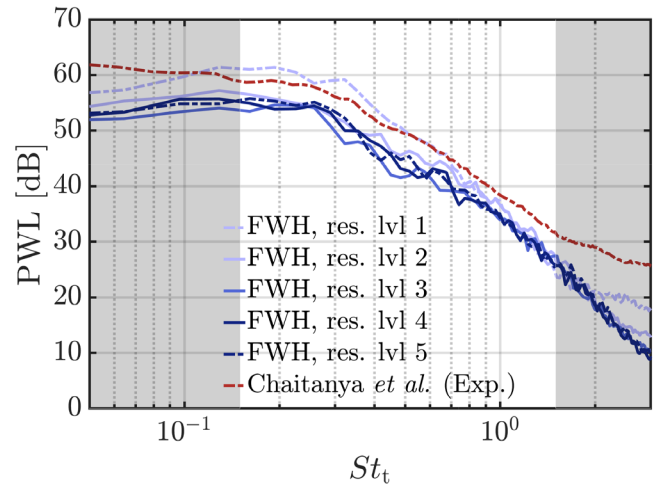

FIG. 3. Grid-independence study in terms of PWL for the different grid resolutions for the NACA-0012 case.

experimental campaign. The trends obtained for the different grid resolutions almost overlap up to $St_t = 2.5$, demonstrating that the results are grid independent in the range of interest from resolution level 3. For $St_t > 2.5$, the effects related to the different resolutions are more evident, particularly for resolution levels 1 and 2. This is due to the coarser refinement around the airfoil surface, where the unsteady pressure used to apply the FWH analogy is sampled.

The convergence trends of $\overline{C}_L$ and $\overline{C}_D$ are shown in Fig. 4 with respect to the total amount of voxels expressed in logarithmic scale. The trend of the drag coefficient indicates that convergence has also been reached in terms of aerodynamic forces at resolution level 4. Conversely, the lift coefficient tends to a constant value as the resolution increases but does not converge to zero, as it would be expected for a symmetric airfoil placed at a 0° angle of attack. A small incidence is likely due to the highly turbulent flow in which the airfoil is immersed and to the slight upward deflection of the flow at the exit of the open-jet wind tunnel. This hypothesis is corroborated by the results of the turbulence characterization in Appendix C, which shows that the time-averaged upwash velocity component is non-zero at the airfoil position. However, this effect is deemed negligible, as it corresponds to a variation of the angle of attack estimated from the lift curve of a NACA 0012 airfoil at the current Reynolds number of approximately 0.25° and does not affect the analysis presented herein.

In view of the above, it can be concluded that convergence has already been achieved at resolution level 4. Consequently, this resolution level has been selected to carry out the investigation for NACA 0012 and for the simulation of NACA 0012-103, considering the excessively high computational cost required to run a simulation at resolution level 5.

B. Validation of the numerical simulations

The validation study is performed by comparing the aerodynamic and acoustic results obtained in the configurations at resolution level 4 of the two airfoils with the data from the reference experimental campaign of Chaitanya et al.[22] For the aerodynamic validation, the flow at
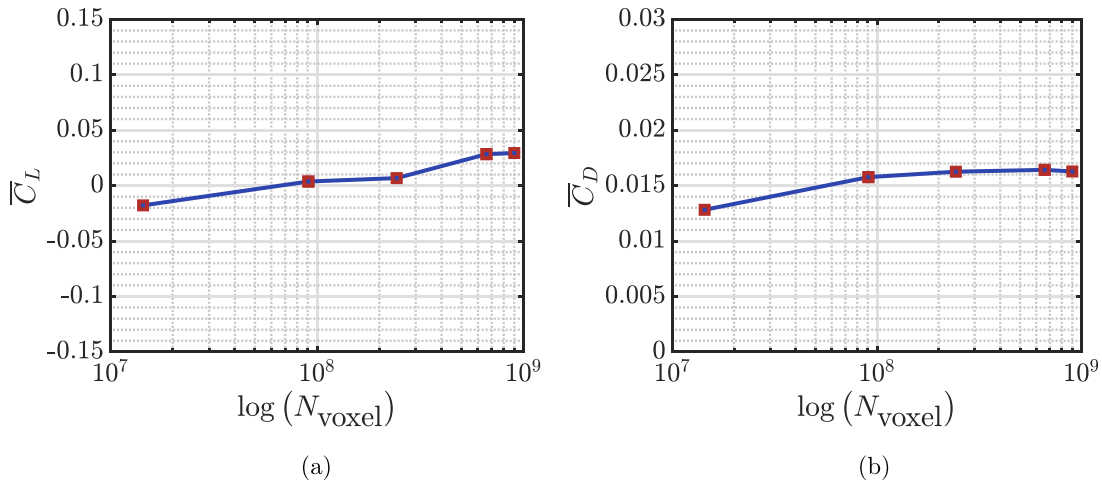
TABLE III. Comparison of the simulation characteristics for the NACA-0012 configuration.

Resolution level	Resolution (r_{LE}/finest voxel)	Total amount of voxel (−)	CPU time (h)
1	3.31	14×10^6	0.80×10^3
2	6.62	91×10^6	7.48×10^3
3	9.93	287×10^6	24.99×10^3
4	13.25	660×10^6	44.75×10^3
5	26.50	900×10^6	96.58×10^3

FIG. 4. Grid-independence study in terms of time-averaged (a) lift coefficient $\overline{C}_L$ and (b) drag coefficient $\overline{C}_D$ for the different grid resolutions for the NACA-0012 case.

the nozzle exit has been assessed in terms of streamwise integral length scale, turbulence intensity, and turbulence frequency spectrum of the streamwise velocity component at $x/c = -0.033$ upstream of the position of the leading edge. The flow characterization has been carried out by running a simulation in which the airfoil is removed while keeping the resolution and the refinement regions unaltered. By sampling the velocity components at this position, a time-averaged free-stream velocity of $\overline{U}_\infty = 59.5\,\text{ms}^{-1}$ and a turbulence intensity $Tu_u = \sqrt{\overline{u'^2}}/\overline{U}_\infty$ of 2.2% are obtained. The streamwise integral length scale is equal to $L_{uu}^x = 6.0 \times 10^{-3}$ m, and it has been estimated using the expression[66]

$$L_{ij}^m(\boldsymbol{x}, l) = \int_0^\infty R_{ij}^m(\boldsymbol{m})\mathrm{d}l = \int_0^\infty \frac{\overline{u_i(\boldsymbol{x} + l\boldsymbol{e}_m)u_j(\boldsymbol{x})}}{\overline{u_i(\boldsymbol{x})u_j(\boldsymbol{x})}}\mathrm{d}l. \quad (4)$$

$R_{ij}^m(x)$ is the correlation coefficient calculated considering a reference location x, u_i, and u_j are the turbulent velocity fluctuations components in the ith and jth directions, respectively, e_m is the unitary vector in the mth direction, and $l = \boldsymbol{l} \cdot \boldsymbol{e}_m$ is the separation length from the reference location. $\overline{\cdot}$ is the temporal-averaging operator with the assumption that the turbulent fluctuations in the open jet are ergodic. The expression has been applied using a discrete integration with respect to the streamwise velocity component, and the calculation is independent of the spatial separation between the sampling points. The values calculated for these quantities are compared with the results obtained in the reference experimental work of Chaitanya et al.[22] The comparison is reported in Table IV, where a good agreement is shown between the turbulence characteristics of the reference experimental campaign and those obtained in the present numerical simulation.

The same values are subsequently used to scale the von Kármán wavenumber spectra for the streamwise and upwash velocity components, using the expressions

$$\Theta_{uu}(k_x) = \frac{1}{\sqrt{\pi}} \frac{\Gamma(5/6)}{\Gamma(1/3)} \frac{\overline{u^2}}{k_e} \frac{1}{\left[1 + (k_x/k_e)^2\right]^{5/6}}, \quad (5)$$

$$\Theta_{vv}(k_x) = \frac{2}{27\sqrt{\pi}} \frac{\Gamma(5/6)}{\Gamma(7/3)} \frac{\overline{v^2}}{k_e} \frac{3 + 8(k_x/k_e)^2}{\left[1 + (k_x/k_e)^2\right]^{\frac{11}{6}}}, \quad (6)$$

where $\Gamma(\cdot)$ is the Gamma function, k_x is the wavenumber in the streamwise direction, and k_e is defined as the wavenumber scale of the largest eddies according to the expression[67]

$$k_e = \frac{\pi}{L_{uu}^x} \frac{\Gamma(5/6)}{\Gamma(1/3)}. \quad (7)$$

The comparison of the von Kármán spectrum scaled with the quantities sampled at $x/c = -0.033$ and the turbulence frequency spectrum acquired at the same position is reported in Fig. 5. The turbulence spectra of the streamwise velocity component have also been compared with the results provided in the reference experimental work [Fig. 5(a)]. The sampled spectrum and the analytical computation are indeed very similar, while the difference with the von Kármán spectrum obtained in the experimental campaign is most likely due to the slight discrepancy in the integral length scale and turbulence intensity.

The analysis of the upwash velocity component spectrum, reported in Fig. 5(b), has been carried out considering just the turbulence frequency spectrum sampled at $x/c = -0.033$ and the von Kármán spectrum scaled with the quantities sampled at this location. This has been scaled using a value for the turbulence intensity of the upwash velocity component $Tu_v = \sqrt{\overline{v'^2}}/\overline{U}_\infty$ equal to 2.8%. No information regarding the upwash velocity component, either in terms of the frequency spectrum and turbulence intensity, is reported in the

TABLE IV. Nozzle open-jet flow characterization. Data are sampled at $x/c = -0.033$ with respect to the origin of the reference system (coincident with the leading edge of the airfoil) and compared with the measurements of the reference experimental campaign by Chaitanya et al.[22]

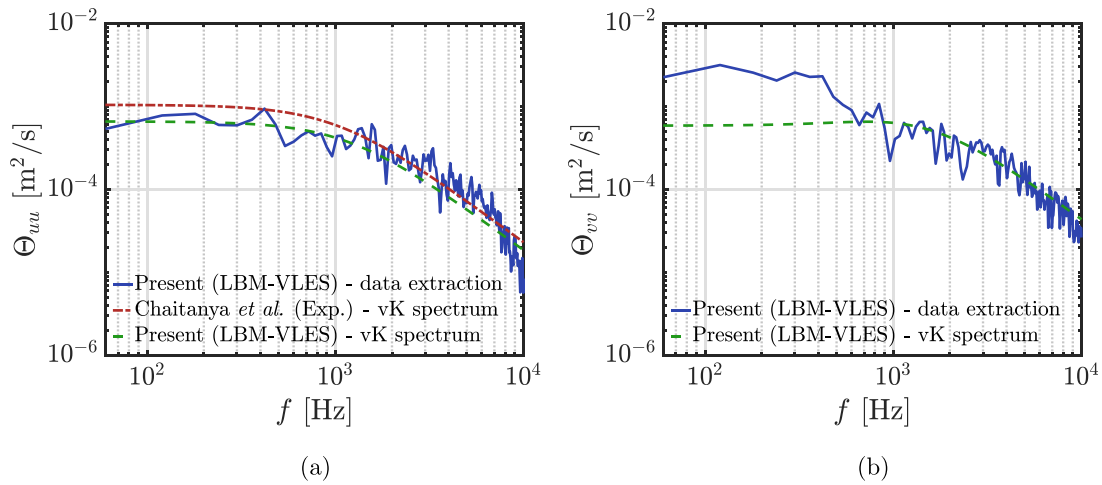|	$\overline{U}_\infty$ (m s^{-1})	Tu_u (%)	L_{uu}^x (m)
Present (LBM-VLES)	59.5	2.2	6.0×10^{-3}
Chaitanya et al.[22] (Exp.)	60	2.5	7.5×10^{-3}

FIG. 5. Power spectral density of the streamwise velocity component acquired at $x/c = -0.033$ with respect to the position of the leading-edge. The spectrum is compared with the von Kármán (vK) spectrum scaled using the integral length scale $L_{uu}^x = 6.0 \times 10^{-3}$ m and the turbulence intensity $Tu_u = 2.2\%$ calculated at the same position. The streamwise component spectra are also compared with the von Kármán spectrum scaled with the results of the reference experimental campaign of Chaitanya et al.[22] ($L_{uu}^x = 7.5 \times 10^{-3}$ m; $Tu_u = 2.5\%$).

reference experimental work of Chaitanya et al.[22] A good agreement is observed between the numerical turbulence spectrum and the analytical one, in particular for frequencies above 1 kHz. In the low-frequency range, the von Kármán spectrum clearly underestimates the trend of the numerical spectrum. This suggests that the turbulent flow features a slight anisotropy, which is most likely due to the strong section contraction in the final part of the nozzle and to the fluctuations induced in the flow by the two shear layers developing on the upper and lower sides of the exit section. As the homogeneity and the isotropy of the incoming turbulence are not necessary conditions for the present investigation, turbulence characteristics will be further detailed for the sake of completeness in Appendix C.

The acoustic validation is performed in terms of PWL and overall sound pressure level (OASPL) directivity patterns. The noise prediction obtained using the FWH analogy along the arc where the direct microphones are placed has been compared with the experimental data, which deployed 18 microphones on an arc spanning from $\theta = \pi/4$ to $3\pi/4$ with a radius R = 1.2 m. The comparison of the PWL is shown in Fig. 6 as a function of the Strouhal number calculated with respect to the airfoil thickness St_t. Additionally, the computational aeroacoustics (CAA) results obtained in the work of Chaitanya et al.[22] are shown for the sake of completeness. For both the airfoils, a 3 dB variation is achieved in the frequency range going from $St_t \simeq 0.15$ to 1.5, where leading-edge noise dominates. An error margin of ± 2 dB has been considered for the measurements, as indicated by
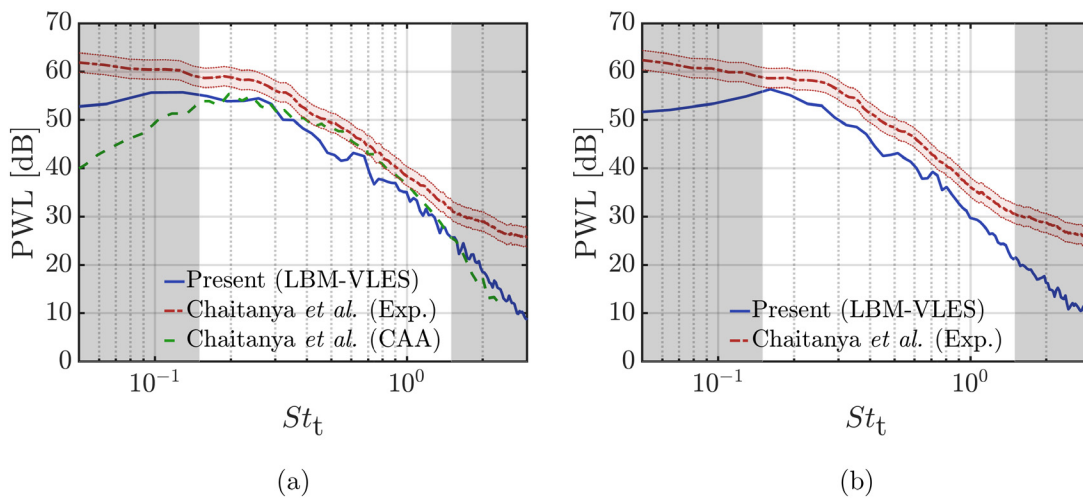

FIG. 6. Acoustic validation for the (a) NACA 0012 and (b) NACA 0012-103 configurations in terms of sound power level.
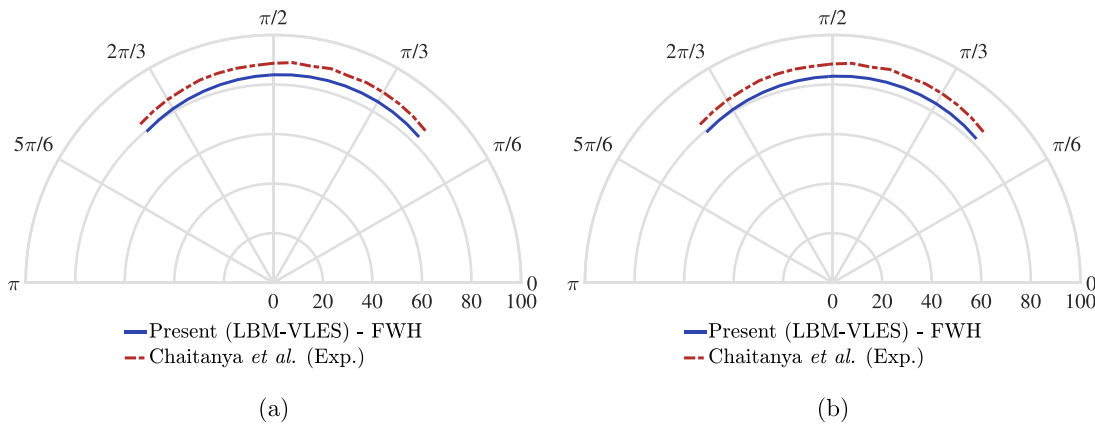
FIG. 7. Acoustic validation for the (a) NACA 0012 and (b) NACA 0012-103 configurations in terms of noise-directivity pattern.

the authors of the experimental campaign. The slight underprediction observed can be attributed to the lower values of the turbulence intensity and the free-stream velocity obtained in the simulation with respect to the experimental values.

A similar satisfactory agreement between the numerical simulations and the measurements is observed in Fig. 7, where the OASPL directivity patterns are shown. The OASPL has been determined by integrating the frequency range going from $St_t = 0.15$ to 1.5.

IV. RESULTS

A. Analysis of the velocity field

The behavior of the turbulent field approaching the airfoil and the extension of the region where distortion occurs can be identified by considering the root mean square of the velocity components along

the stagnation streamline. Figure 8 shows the trends for the streamwise and upwash velocity components u and v for the NACA 0012 and the NACA 0012-103 airfoils (the spanwise velocity component w is not shown, as its fluctuations remain constant, as also confirmed by Hunt[31]). As the flow approaches the stagnation point, the blockage induced by the body causes the streamwise velocity fluctuations to abruptly decrease and the upwash fluctuations to increase.[31] This distortion mechanism prevails in the case of large-scale turbulence, i.e., when the ratio of the scale of the incoming turbulence to the characteristic dimension of the body, identified in the literature as the airfoil leading-edge radius (see Sec. I), is greater than 0.5.[68] This is the case for two airfoils under investigation: L^x_{uu}/r_{LE} amounts to 2.5 and 1 for NACA 0012 and NACA 0012-103, respectively.

Notably, the trends of the root mean square of the velocity components along the stagnation streamline coincide both far away and in
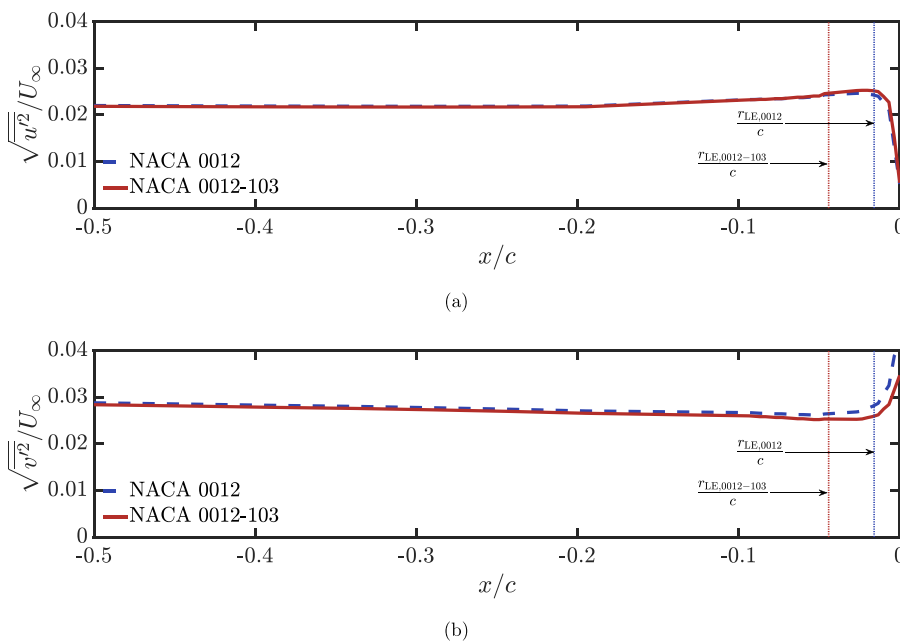

(a)

(b)

FIG. 8. Comparison of the root mean square of the spanwise-averaged (a) streamwise and (b) upwash velocity components along the stagnation streamline for the two airfoil configurations. The dashed lines highlight the position corresponding with one leading-edge radius upstream of the leading edge for both cases.
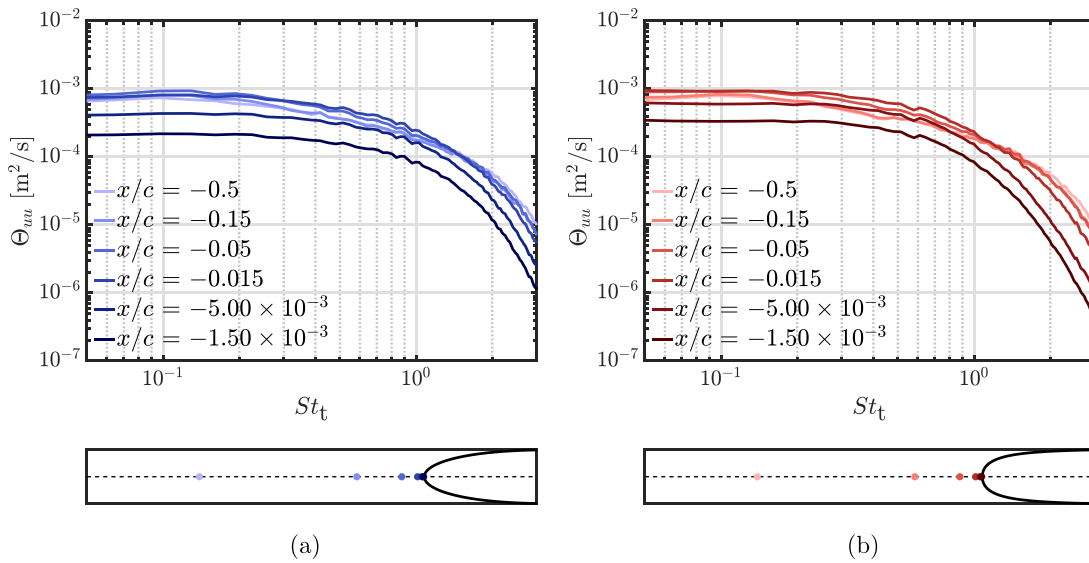
FIG. 9. Turbulence frequency spectra of the streamwise velocity component along the stagnation streamline at different distances from the airfoil leading edge for the (a) NACA 0012 and the (b) NACA 0012-103. All the spectra are spatially averaged in the spanwise direction.

the vicinity of the stagnation point, despite the significant difference between the two leading-edge radii. The variation due to the presence of the body occurs at a distance from the stagnation point that appears unrelated to the leading-edge radius. These findings differ from those of Mish and Devenport[36,37] and De Santana et al.,[40] according to whom turbulence-distortion effects are detected within $1r_{LE}$ from the stagnation point, and challenge the relevance of this geometrical parameter in the alteration of the velocity field.

Further indications about the alteration of the velocity field due to the deformation of the turbulent structures are provided by the velocity spectra at different positions along the stagnation streamline. Figure 9 reports the spectra of the streamwise velocity component Θ_{uu} at six different upstream locations from the stagnation point, listed in the legend of the figure. Data are spatially averaged in the spanwise direction. The turbulence frequency spectra for both airfoils overlap up to $x/c \simeq -5 \times 10^{-3}$, while, for smaller distances, the effects caused by the presence of the body start to be apparent, i.e., Θ_{uu} decreases for all the frequencies.

The same analysis is also repeated for the upwash velocity component, whose turbulence frequency spectra Θ_{vv} are reported in Fig. 10. Notably, for both airfoils, the variation of Θ_{vv} approaching the stagnation point differs from that of the spectra of the streamwise velocity. In this case, the amplitude of the low-frequency part increases, whereas that for the high-frequency part decreases. These two different trends depend on the ratio L_x/a, which is related to the leading-edge geometry, as explained in Sec. I. The crossover frequency between the two trends thus indicates the wavelength at which they balance each other, corresponding to turbulent structures similar in size to the characteristic dimension of the obstacle. This explains why the crossover frequency is observed at $St_t \simeq 1$ in the case of NACA 0012 [Fig. 10(a)], which features a sharper leading edge, while it is slightly lower, around $St_t \simeq 0.6$, for the more rounded NACA 0012-103 [Fig. 10(b)]. Finally, at locations along the stagnation streamline where turbulence is already distorted, the low-frequency part of the spectrum

does not change significantly with the decreasing distance from the surface, while the slope of the high-frequency part keeps increasing.

Since the high-frequency attenuation has been identified as the most significant effect on the airfoil aerodynamic and acoustic response in the presence of a realistic airfoil geometry, it is worth focusing on the decay slopes of the spectra at different distances from the leading edge, also depicted in the plots of Fig. 10. For large distances from the leading edge, i.e., $|x/c| > |-0.015|$, the decay slope is $-5/3$, as foreseen by the linearized theory for the inertial subrange.[67] For the spectrum sampled at $x/c = -0.015$, it is still close to $-5/3$ but progressively decreases as the stagnation point is approached. At $x/c = -5 \times 10^{-3}$, Θ_{vv} is characterized by a decay slope of $-10/3$ for both airfoils. This value is predicted by the RDT for spectra in the vicinity of the leading edge but for angular positions away from the stagnation streamline.[31] The spectra sampled closest to the body for both airfoils feature a steeper *exponential* decay slope, for which the following expression derived by Hunt[31] for the normalized Θ_{vv} in the immediate vicinity of the stagnation point reads

$$\frac{\Theta_{vv}}{u'^2 L_x} \simeq G_1 \left(a/L_x\right)^{-\frac{2}{3}} \kappa^{-\frac{7}{3}} e^{-\frac{1}{2}\pi\kappa}, \tag{8}$$

with $\kappa = a\,k_x$ being the wavenumber non-dimensionalized with respect to the characteristic size of the body and where

$$G_1 = \frac{55 \times 0.1955 \times \pi^{\frac{1}{2}} \Gamma\left(\frac{1}{3}\right) \Gamma\left(\frac{5}{3}\right)}{36\pi \times 4\pi \times \left(\frac{3}{4}\right)^{\frac{5}{3}} \Gamma\left(\frac{11}{6}\right)} = 0.0566.$$

In this case, the characteristic size of the body a has been set equal to the geometrical parameter l_{dis}, which will be introduced in the subsection Sec. IV C. For further details about the analytical derivation of this expression, the reader can refer to Secs. 5 and 6 of Hunt.[31]
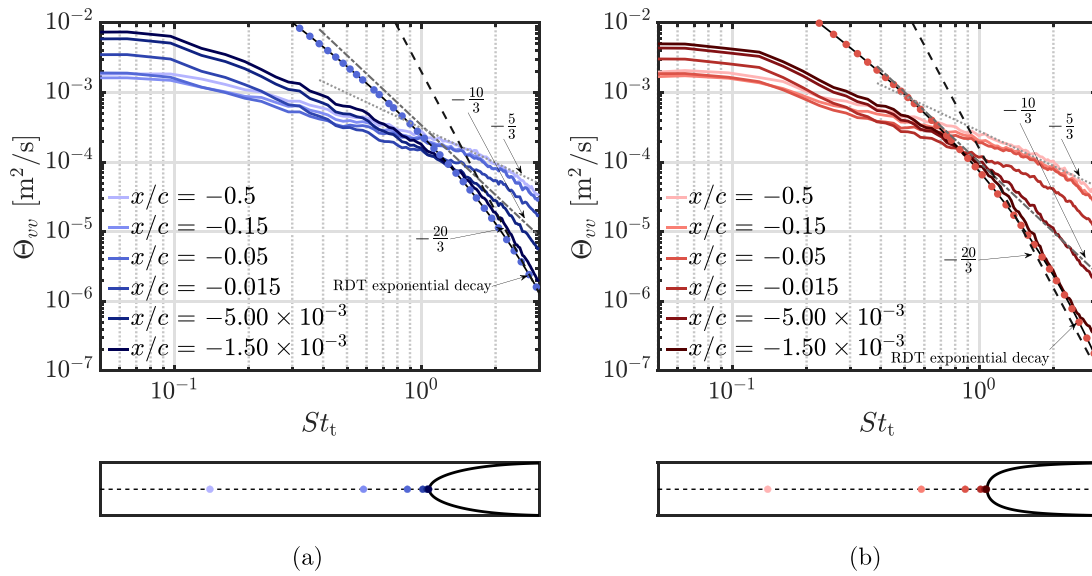
FIG. 10. Turbulence frequency spectra of the upwash velocity component along the stagnation streamline at different distances from the airfoil leading edge for (a) NACA 0012 and (b) NACA 0012-103. All the spectra are spatially averaged in the spanwise direction.

Interestingly, in the frequency range of analysis, this exponential decay can be approximated by a linear decay with a slope of $-20/3$.

The spanwise evolution of turbulence as the airfoil leading edge is approached is analyzed in terms of spanwise coherence length $l_z(\omega)$ using Eq. (A13), which is linked to the inflow-turbulence noise produced by the airfoil, as shown in Eq. (A12). The coherence of the upwash velocity component in the spanwise direction is calculated at the locations listed in the legend of the figure along the stagnation streamline. Results, which are reported in Fig. 11, show that the $l_z(\omega)$ values in the low-frequency range increase as the stagnation point is approached, whereas

the high-frequency range is not affected by the turbulence distortion and does not vary with the increasing proximity to the leading edge.

B. Turbulence-distortion effects on unsteady surface pressure

Relevant indications about the noise-generation mechanism and effect of airfoil geometry can be inferred by looking at the pressure distribution on the airfoil surface. The root mean square of the spanwise-averaged surface-pressure fluctuations, which are normalized by the
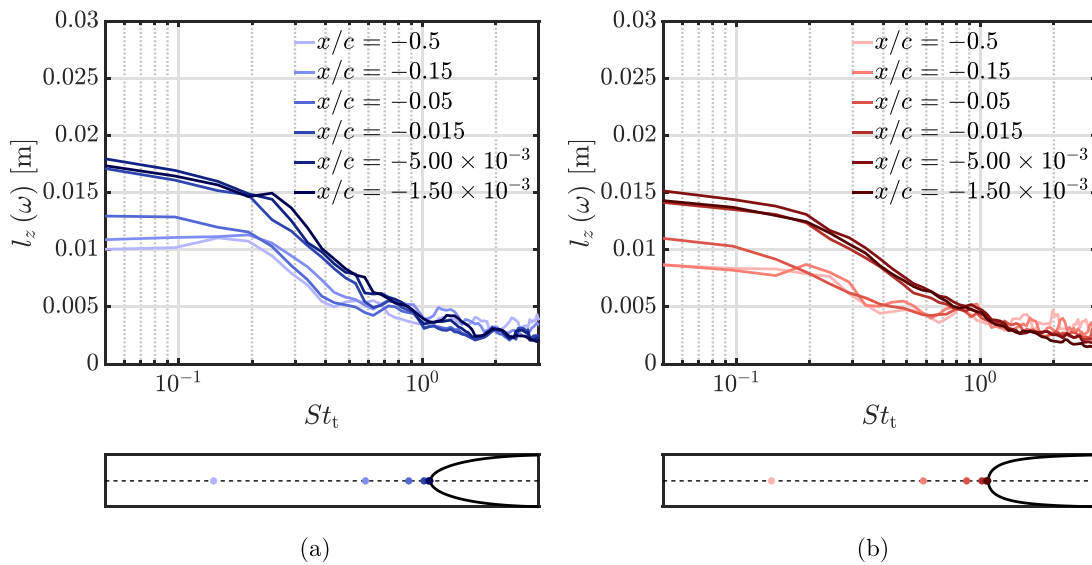

FIG. 11. Spanwise coherence length of the upwash velocity component along the stagnation streamline at different distances from the airfoil leading edge for (a) NACA 0012 and the (b) NACA 0012-103.

free-stream dynamic pressure q_∞, is shown for both airfoils in Fig. 12. The distributions, reported as a function of the curvilinear abscissa s, are compared to the spatial derivative with respect to s of the time-averaged pressure coefficient C_p along the surface. For both airfoils, the position along the surface at which the pressure fluctuation is maximum occurs downstream of the stagnation point, in agreement with the results of Zamponi *et al.*[69] More precisely, the point of maximum surface-pressure fluctuations is slightly downstream of the position where the pressure gradient peaks. This result suggests a direct relation between the pressure gradient along the airfoil, which is associated with the mean flow around the body, and the spatial distribution of the surface-pressure fluctuations, which are connected with the noise-generation efficiency of the body.[43]

The distributions of these quantities are also compared with the spatial derivative of the non-dimensional curvature C_s with respect to the curvilinear abscissa s [Figs. 12(c) and 12(d) for NACA 0012 and NACA 0012-103, respectively]. As expected, the pressure gradient is maximum where the curvature changes more abruptly, i.e., at the position where the derivative of the curvature reaches its utmost. This

observation identifies in the *variation* of curvature, which is related to the sharpness of the leading edge, a relevant geometrical feature for noise-generation efficiency, as also shown by Lockard and Morris,[17] Oerlemans,[20] Moriarty *et al.*[70] Indeed, even though the far-field noise spectra for the two airfoils are comparable (see Fig. 6), a slight noise reduction of around 5 dB occurs for NACA 0012-103, which is characterized by a more rounded leading edge, for $St_t > 0.6$. This is attributed to the lower peak (around 80%) of the surface-pressure fluctuations with respect to that induced on NACA 0012 (see Fig. 12), confirming that the shape of the leading edge has an impact on the sound-radiation efficiency of the airfoil even when the thickness is kept constant, in agreement with Gill *et al.*[24] In addition, the pressure-gradient intensity, associated with the variation of curvature in the front part of the airfoil, seems to affect the distortion of the turbulent structures as they accelerate along the surface, as also concluded by Gershfeld.[27]

The impact of the alteration of the velocity field due to turbulence distortion on the noise generation is investigated by analyzing the frequency spectra of the pressure fluctuations at different positions along
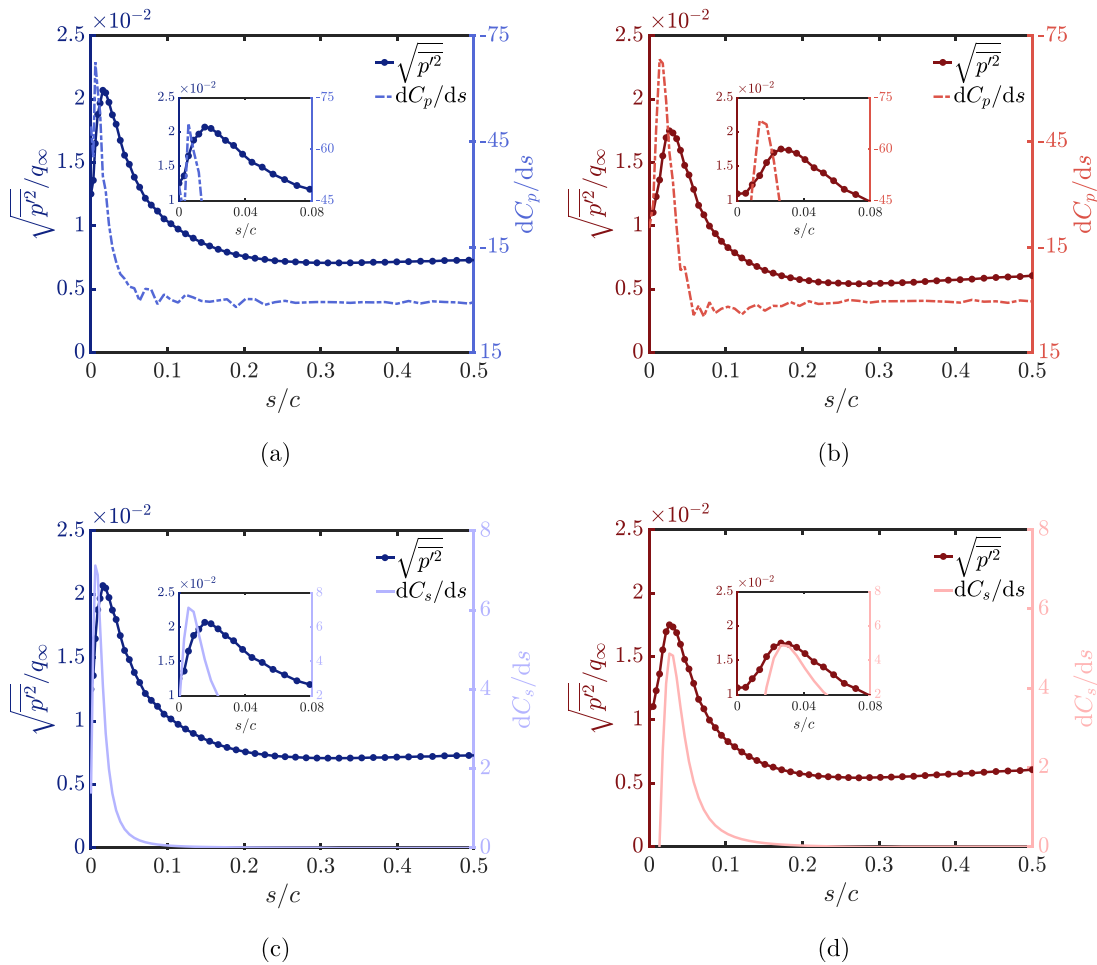

FIG. 12. Analysis of the surface pressure. The root mean square of the surface-pressure fluctuations is compared with the time-averaged pressure gradient and the derivative of the curvature of the leading edge of the airfoil for (a)–(c) NACA 0012 and (b)–(d) NACA 0012-103.

the surface of the airfoils and averaged in the spanwise direction (Fig. 13). The five sampling locations are set as multiples of the curvilinear abscissa of the point of maximum pressure fluctuations with respect to the stagnation point, defined as l_{dis}. The purpose is to analyze the variation of surface-pressure characteristics in the surroundings of the point where the noise source is maximum. For both NACA 0012 and NACA 0012-103, the surface-pressure spectra in the vicinity of the leading edge feature an exponential decay slope in the high-frequency range. Such decay is caused by the pileup of the vortical structures on the stagnation point, which leads to a more effective cancelation of the pressures induced by the eddies with respect to other positions around the body.[71] At the stagnation point and in the high-wavenumber asymptotic limit, which describes the effects on the surface pressure caused by the distortion of small-scale structures, this physical mechanism can be modeled by[71]

$$\Theta_{pp} \propto (a/L_x)^{-\frac{2}{3}}(L_x\kappa/a)^{-\frac{7}{3}}e^{-\pi\kappa Q}. \qquad (9)$$

Here, Q is a factor derived from the expansion of Lighthill's drift function[72] computed on the surface boundary, which the linearized theory estimates to be $O(1)$. This parameter has been determined by matching the exponent to that of the high-frequency exponential decay of the upwash velocity spectrum identified by Hunt,[31] resulting in $Q = 0.6$ for both airfoils. Under this assumption, Fig. 13 shows that the analytical calculations correctly approximate the surface-pressure spectra sampled at the closest positions to the stagnation point for both airfoils, proving that, in the vicinity of the leading edge, the unsteady surface pressure in the high-frequency range decays as the upwash velocity. Moreover, similarly to the velocity field, the exponential roll-off characterizing the high-frequency range of the surface-pressure spectrum is very close to a linear decay with a slope of $-20/3$. This result agrees with the experimental findings of Bowen et al.,[25] who showed that the high-frequency slope of the surface-pressure PSD in the vicinity of the stagnation point of a NACA 0012 scales

approximately with the 7th power of the frequency. As the surface-pressure spectra are sampled more downstream, a significant reduction in the absolute value of the decay slope and amplitudes at high frequencies is observed, whereas the levels in the low-frequency range increase up to the location of maximum surface-pressure fluctuations and then decrease.

The effects of the distorted velocity field on the surface-pressure distribution are now studied in terms of coherence $\gamma^2_{v'p'}$ between the surface pressure and the upwash velocity sampled at two different locations along the stagnation streamline using Eq. (A14). Figure 14 shows the $\gamma^2_{v'p'}$ distribution along the airfoil using as reference points $x/c = -0.5$ and -1.5×10^{-3}, i.e., the furthest and closest positions with respect to the leading edge among those previously considered. Higher coherence between the surface pressure on the leading edge and the upwash velocity component is obtained when the velocity is taken very closely to the stagnation point, particularly in the high-frequency range. In agreement with Bowen et al.[25] and Zamponi et al.,[69] the highest $\gamma^2_{v'p'}$ values are found slightly downstream of the stagnation point, specifically at the location where the root mean square of the surface-pressure fluctuations is maximum, i.e., at the position where the curvature changes more abruptly. The high coherence between the surface pressures and upwash velocity fluctuations in the vicinity of the stagnation point confirms that sound-production mechanisms are affected by the alteration experienced by the velocity field due to the distortion of the turbulence structures. Consequently, the investigation of the surface pressure can provide meaningful insight into the deformation mechanisms experienced by the incoming turbulence, as will be demonstrated in Sec. IV C.

C. Description of turbulence-distortion mechanisms and influence of airfoil geometry

The turbulence-distortion mechanism is now further elucidated in view of the results of the analyses of the surface pressure and the
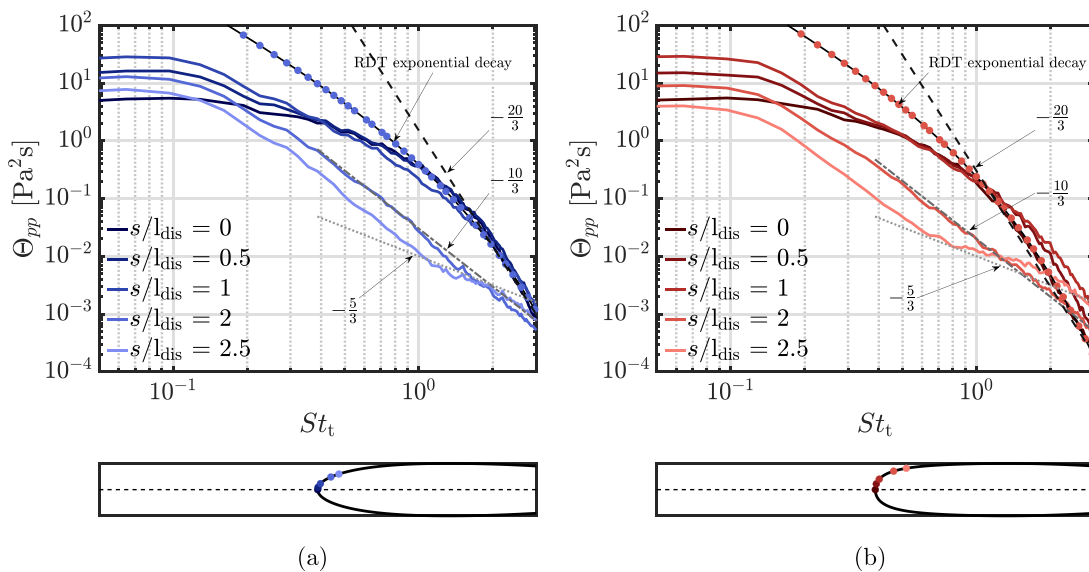

FIG. 13. Surface-pressure spectra at different positions along the airfoil surface for (a) NACA 0012 and (b) NACA 0012-103. All the spectra are spatially averaged in the spanwise direction.
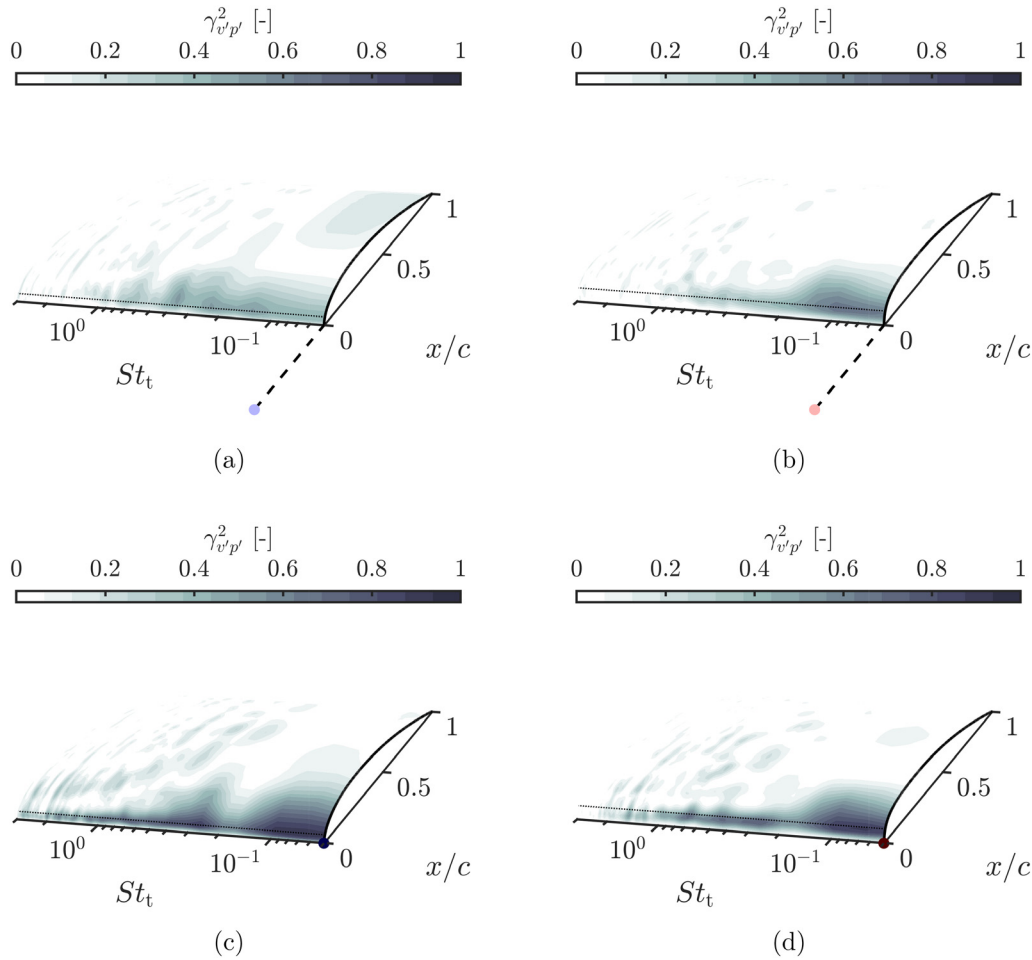
FIG. 14. Coherence between the surface pressure and the upwash velocity sampled at (a) $x/c = -0.5$ and (c) $x/c = -1.5 \times 10^{-3}$ for NACA 0012 and at (b) $x/c = -0.5$ and (d) $x/c = -1.5 \times 10^{-3}$ for NACA 0012-103. In the FIGS, the position where the upwash velocity is sampled is shown with a dot, while the dotted line depicts the position along the airfoil where surface-pressure fluctuations peak.

velocity field. As shown in Sec. IV A, the frequencies marking the crossover between the large-scale distortion behavior (low-frequency part of the spectra) and the small-scale one (high-frequency part of the spectra) differ for the two airfoils. This finding hints at an effect of the leading-edge geometry on the distortion mechanisms of the incoming turbulent structures, which are dictated by the conditions $L_x/a \gg 1$ and $L_x/a \ll 1$.

What remains to be elucidated yet is which geometrical parameter a determines these different behaviors. The evolution of the surface-pressure fluctuations provides a valuable indication for it. Indeed, if turbulence distortion, as well as noise generation, is affected by the flow accelerating along the airfoil surface, it is reasonable to assume that the relative size of the eddies with respect to the space available for accelerating is also relevant in determining the deformation mechanism the eddies will experience in the interaction with the leading edge. As previously mentioned, this distance l_{dis} can be estimated from the geometrical characteristics of the airfoil, being this parameter comparable to the arc length going from the stagnation

point to the position of maximum variation of curvature. This location also coincides with the point where the airfoil geometry at the leading edge starts diverging from the curve of the osculating circle, i.e., $l_{dis} = \theta_{dis}r_{LE}$, with θ_{dis} being the angular position along the leading-edge circle associated with the point of the maximum derivative of the airfoil curvature (Fig. 15).

By employing a Strouhal number $St_{l_{dis}}$ defined with this quantity, the impact of l_{dis} on the distortion of the incoming turbulence structures can be assessed. The turbulent spectra of the upwash velocity component at three different distances from the stagnation point are shown in Fig. 16 for both airfoils. Using $St_{l_{dis}}$, the spectra collapse for all the considered distances, suggesting that the *distortion length* l_{dis} is the geometrical parameter to consider to evaluate the turbulence-distortion effects and legitimate the extension of the RDT results to airfoil applications. This is also a further indication that the leading-edge radius *indirectly* plays a role in the identification of the turbulence-distortion mechanisms via the length of the arc from the stagnation point to the position of maximum curvature. Interestingly, in the case
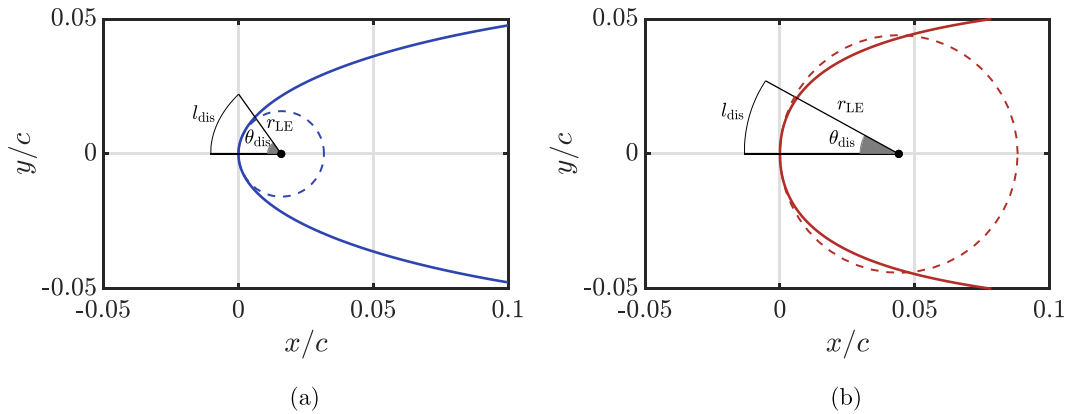
FIG. 15. Geometry of the leading edge of (a) NACA 0012 and (b) NACA 0012-103 with highlighted the parameter l_{dis}, geometrically comparable to the distance along the airfoil surface between the stagnation point and the position of maximum curvature variation.

of NACA 0012, the value of l_{dis} almost coincides with the leading-edge radius, supporting the literature results outlined in Sec. I that considered r_{LE} as the characteristic dimension of the airfoil noise dictating the turbulence distortion.

D. Turbulence-distortion effects on leading-edge noise prediction

The results of the analysis of the velocity field in the vicinity of the leading edge and the unsteady surface pressure on the airfoil allow the assessment of turbulence-distortion effects in low-fidelity models. A first attempt to account for these effects in Amiet's model is carried out by using Eq. (A9), which relates the far-field noise to the cross-spectral density of the surface pressure on the airfoil by means of Curle's analogy. This has been solved by using an in-house routine implemented in MATLAB by MathWorks. The outcome of this implementation of Amiet's model compared to the noise prediction obtained with the solid formulation of FWH analogy is shown in Fig. 17 in terms of SPL, whose calculation considers the observer above

FIG. 16. Comparison of the upwash velocity component spectra for the two airfoils as a function of the Strouhal number defined using the quantity l_{dis}, which represents the arc length along the surface for which the airfoil is approximated as a circle.

the leading edge ($\theta = \pi/2$) at a distance of R = 1.2 m. The noise prediction obtained with Amiet's model coincides with the results of the FWH analogy, correctly estimating the noise levels and the decay slope in the range of interest, up to the frequency associated with the sampling spatial resolution of the surface pressures in Amiet's model. Indeed, this resolution was kept significantly lower than that employed by PowerFLOW for the FWH analogy due to the excessive computational cost required by solving Eq. (A9) in MATLAB. This results in an insufficient characterization of destructive interference effects, which explains the discrepancy observed at very high frequencies.

The comparison, on the one hand, shows that the analytical model of Amiet is able to accurately predict inflow-turbulence noise also for the case of airfoils with non-negligible thickness but, on the other hand, is not particularly interesting from an applicative point of view since its implementation requires the knowledge of the surface pressure field on the whole airfoil. The advantage of using a low-fidelity method to decrease the computational cost would be, hence, lost.

The most relevant and practically useful formulation of Amiet's model is that of Eq. (A10), which allows the calculation of the far-field noise starting from the characteristics of the incoming turbulence by using a transfer function to model the response of the airfoil to the perturbation. Given the results obtained in the previous section regarding the modification of the velocity field in the vicinity of the surface, a possible approach to account for the turbulence-distortion effects in the noise prediction by means of Amiet's model is to consider turbulence characteristics in the vicinity of the stagnation point. The simplified version of Eq. (A12) is employed to consider the turbulence spectrum along the stagnation streamline as input. In particular, the $\Theta_{vv}(\omega)$ acquired in the closest position to the airfoil leading edge ($x/c = -1.5 \times 10^{-3}$) is used in the equation. The spanwise coherence length $l_z(\omega)$ is calculated at the same position. The noise prediction obtained using this low-fidelity method is compared to the results of the FWH analogy in terms of SPL and PWL. For the calculation of the SPL, the observer location has been considered to be right above the leading edge ($\theta = \pi/2$) in the midspan plan, at a distance of R = 1.2 m.

The comparison in SPL between the analytical prediction and the FWH analogy is reported in Fig. 18, while Fig. 19 shows the
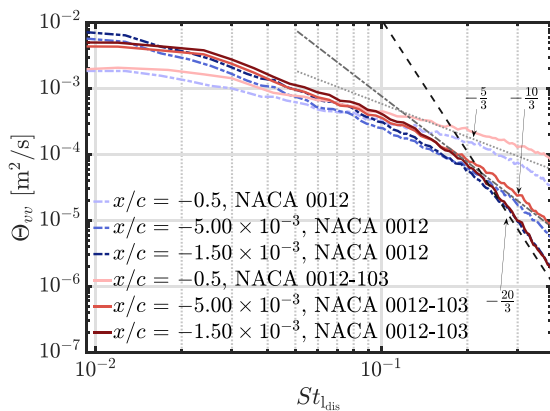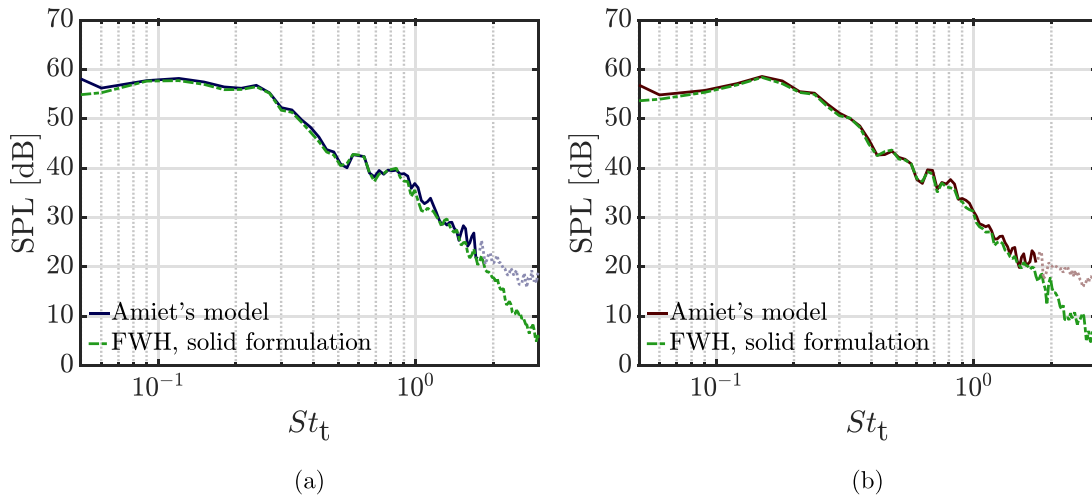
FIG. 17. Sound pressure level in the far-field calculated for an observer placed at R = 1.2 m and $\theta = \pi/2$, with the angular position computed with respect to the downstream direction, for (a) NACA 0012 and (b) NACA 0012-103. Amiet's implementation using surface pressure cross-PSD as input is compared to the calculation provided by the FWH analogy. The reference pressure for the SPL calculation is 2×10^{-5} Pa.

corresponding PWL. Amiet's model using as input the turbulence spectrum sampled 1.5×10^{-3} c upstream of the leading edge, indicated with $\Theta_{vv,\mathrm{dis}}$, is compared with the prediction using a spectrum sampled far upstream as input, i.e., at 0.5 c from the stagnation point, expressed as $\Theta_{vv,\mathrm{ups}}$. In agreement with the literature findings, the canonical application of Amiet's model, i.e., considering a spectrum representing the undistorted conditions, correctly estimates the noise level in the low-frequency range up to $St_t = 0.35$, while overpredicts it for higher frequencies, for which the decay slope of the spectrum is not correctly calculated. Conversely, the prediction of Amiet's model using the distorted spectrum features the same trend as that computed with

the FWH analogy, including the correct decay slope in the high-frequency range. A general overestimation in the entire frequency range is obtained, though. This overestimation is traced back to the results of the velocity-field analysis in the stagnation region, where the upwash velocity spectrum increases in the low-frequency range and decreases in the high-frequency one, and depends on the fact that the aeroacoustic transfer function in Eqs. (B7) and (B8) have not been modified accounting for the distortion effects. Given the crucial role played by the transfer function in the quantitative prediction of the emitted noise levels, Sec. IV E will be dedicated to investigating these effects.
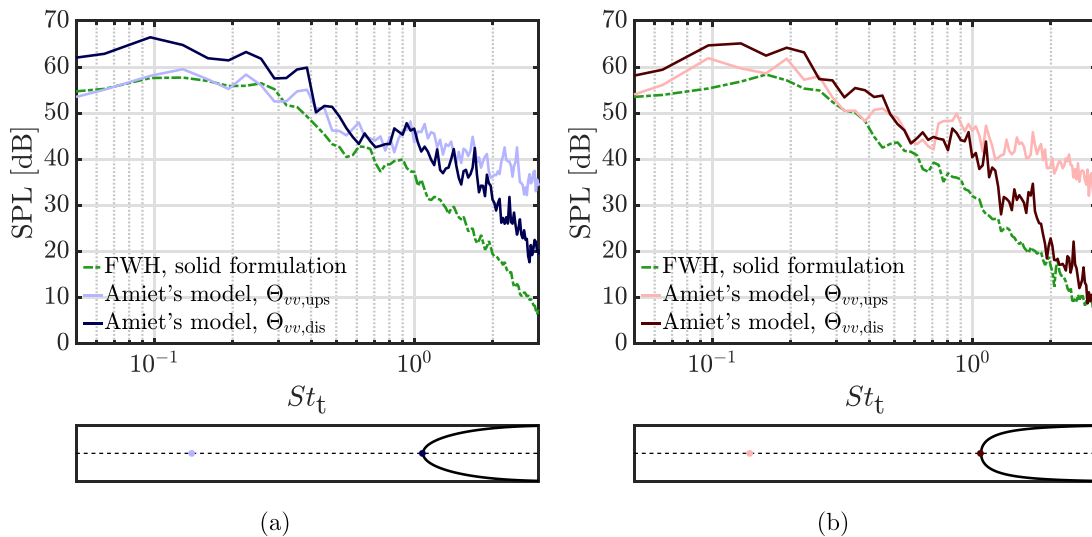

FIG. 18. Sound pressure level in the far-field calculated for an observer placed at R = 1.2 m and $\theta = \pi/2$, with the angular position computed with respect to the downstream direction, for (a) NACA 0012 and (b) NACA 0012-103. Amiet's implementation using spectra sampled far upstream $\Theta_{vv,\mathrm{ups}}$ and in the distorted region of the flow field $\Theta_{vv,\mathrm{dis}}$ is compared to the calculation provided by the FWH analogy. The reference pressure used to calculate the SPL is 2×10^{-5} Pa.
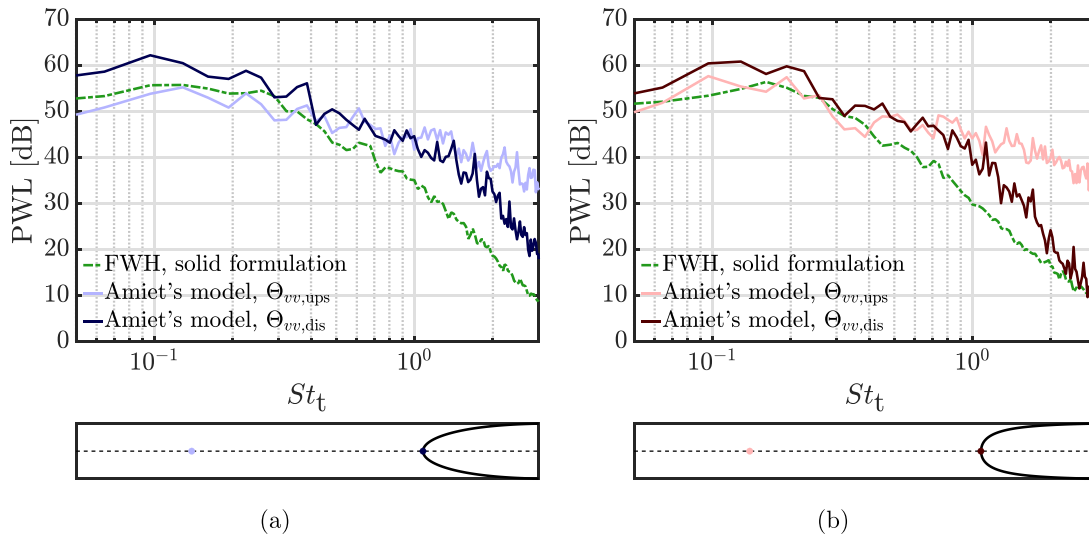
FIG. 19. Sound power level in the far-field for (a) NACA 0012 and (b) NACA 0012-103. Amiet's implementation using spectra sampled far upstream $\Theta_{vv,\text{ups}}$ and in the distorted region of the flow field $\Theta_{vv,\text{dis}}$ is compared to the calculation provided by the FWH analogy. The reference power used to calculate the PWL is 10^{-12} W.

The consequences of incorporating turbulence-distortion effects into Amiet's model are now evaluated by varying the sampling position of the turbulence spectrum across the entire stagnation region. The analysis involves calculating the difference in the overall sound pressure level ΔOASPL between Amiet's model using the distorted spectrum as input and the results provided by the FWH analogy. The difference between these two noise predictions has been calculated in the frequency range in which leading-edge noise prevails, i.e., $0.15 < St_\text{t} < 1.5$.

It is useful to combine such analysis with the assessment of the difference in decay slope in the high-frequency range $|\Delta m|$ between the spectrum obtained with the FWH analogy and Amiet's model with different positions where Θ_{vv} is sampled. The decay slopes of the sound power levels in the range going from $St_\text{t} = 0.4$ to 2 are taken as reference. Figure 20 reports the contour plot of both these quantities for the two airfoils. On the one hand, the results for the ΔOASPL in Figs. 20(a) and 20(b) demonstrate that a substantial increase in terms of noise levels up to 6 dB in comparison with the numerical simulations is obtained by sampling Θ_{vv} closer to the stagnation point. On the other hand, the difference in decay slope between Amiet's model and FWH shown in Figs. 20(c) and 20(d) indicates that a significant improvement is achieved in the high-frequency range with respect to the canonical application of Amiet's model, with Δm tending to zero when the turbulence spectrum is sampled at the airfoil stagnation region.

E. Aeroacoustic transfer function modification for distorted-turbulence input

In view of the above, the effects of turbulence distortion on the velocity field must be taken into account in the physical modeling of the noise-generation mechanism at the basis of low-fidelity noise-prediction methods. The constant noise overestimation across the entire frequency range, however, indicates that the effects of turbulence distortion have not been fully accounted for. Indeed, the comparison with the accurate prediction obtained implementing Eq. (A9), which does not require a transfer function to relate the unsteady loading distribution to the incoming turbulence characteristics, suggests that potential distortion effects on the airfoil response modeling must be assessed.

As outlined in Appendix A, Amiet's model relies upon the relation between the pressure distribution on the airfoil surface (specifically, a flat plate) and the upstream incident gust that induces the unsteady loading. The analytical expression for this relation [Eq. (A2)] is obtained in the assumption of monochromatic sinusoidal gust with amplitude v_0 [Eq. (A1)], which introduces the transfer function $g(x, k_x, k_z)$. Employing a transfer function based on the response of a flat plate is equivalent to following a *quasi-steady* theory, which is based on the hypothesis that the only effect of turbulence added to the incoming flow is a small change in the angle of incidence and magnitude of the upstream velocity.[71] This corresponds to assuming the surface pressure on the flat plate to be induced by undistorted large-scale turbulence. Nevertheless, it has been shown in Sec. IV A that, for both airfoils, the realistic geometry effects entail a variation of the turbulent velocity as the stagnation point is approached due to the blockage caused by the surface (see Fig. 8). This variation in the energy content, which can also be interpreted as an increase in the perturbation amplitude, supports the increase in the low-frequency range observed for upwash-velocity spectra sampled in the stagnation region, which is related to the distortion of large-scale turbulent structures. However, the original formulation of the transfer function does not encompass this energy increase, explaining the observed overestimation once the altered turbulence spectrum is used in the prediction. This can be shown by applying the same analytical procedure followed by Amiet but considering a sinusoidal gust $v_\text{dis}(x, z)$ with amplitude scaled of a factor α_dis with respect to the upstream undistorted one v_0 as input

$$v_\text{dis}(x, z) = (\alpha_\text{dis} v_0)e^{i[k_x(U_\infty t - x) - k_z z]} = \alpha_\text{dis}v(x, z). \tag{10}$$

In the framework of the quasi-steady theory, this distorted gust is considered to be mathematically related to the altered turbulence spectrum that accounts for distortion effects.
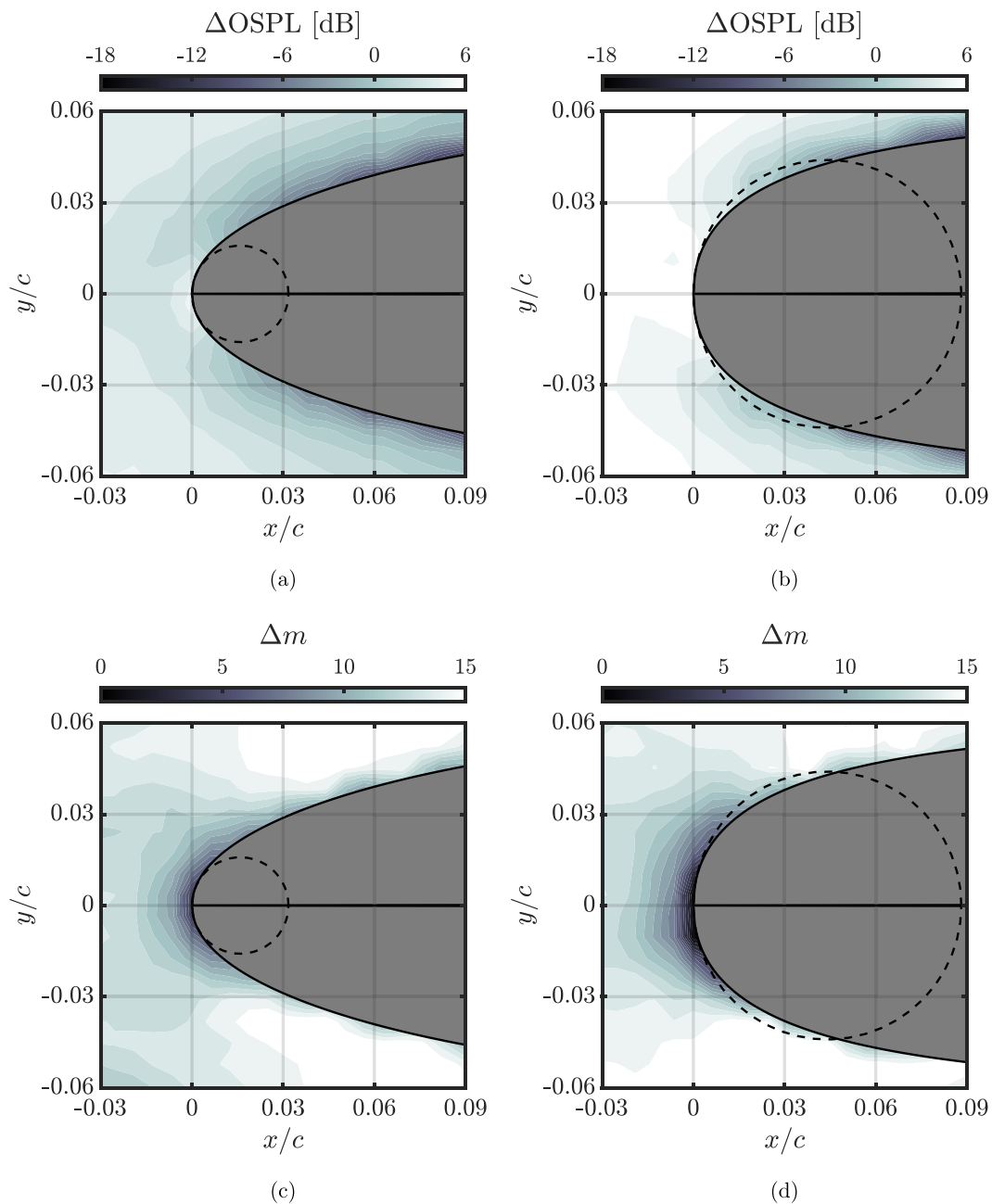
FIG. 20. Difference in overall sound pressure level ΔOASPL and in slope Δm of the PWL between the noise prediction from the FWH analogy and from Amiet's model using different sampling positions for the turbulence spectrum. These quantities are shown respectively in (a) and (c) for NACA 0012 and in (b) and in (d) for NACA 0012-103. For the ΔOASPL, the observer is placed at R $=$ 1.2 m and $\theta = \pi/2$, with the angular position computed with respect to the downstream direction. The slope is calculated in the range $St_t = 0.4$–2.

Note that the terms of the aeroacoustic transfer function do not feature a dependence on the gust amplitude and are not directly affected by its variation. Indeed, as detailed in Appendix B, v_0 cancels out in the calculation of leading-edge term $\mathcal{L}_1$ [Eq. (B7)] and the trailing-edge one $\mathcal{L}_2$ [Eq. (B8)] by substituting the pressure terms induced by the sinusoidal perturbation [Eqs. (B1) and (B2)] in the expression for $g(x, k_x, k_z)$ [Eq. (B6)]. This indicates that the intensity of the aerodynamic and acoustic response of the airfoil depends on the amplitude of the gust term in Eq. (A2) and the turbulence spectrum once the formulation is expressed in statistical quantities. This passage

from time and space-dependent expressions to statistical operators is worth a more detailed analysis. The cross-PSD of the surface pressure in Eq. (A6) is indeed retrieved from Eq. (A5) through

$$S_{QQ}(x_1, x_2, z_1, z_2, \omega) = \lim_{T \to \infty} \frac{\pi}{T} \langle \Delta \hat{p}(x_1, z_1, \omega) \Delta \hat{p}^\dagger(x_2, y_2, \omega) \rangle, \quad (11)$$

with $\langle \cdot \rangle$ indicating the expected-value operator and the superscript $\dagger$ identifying the complex conjugate. At this point, once Eq. (A5) with the distorted gust as input is substituted into Eq. (11), the only non-deterministic quantity is the Fourier transform of the gust $\hat{v}_{R,\mathrm{dis}}(k_x, k_z)$. Taking all the other terms out of the expected value yields

$$\langle \hat{v}_{R,\mathrm{dis}}(K_x, k_z) \hat{v}_{R,\mathrm{dis}}^\dagger(K_x, k_z) \rangle = \frac{R}{\pi} \Phi_{vv,\mathrm{dis}}(K_x, k_z), \quad (12)$$

where the distorted turbulence spectrum used as input in the model appears. Considering Eq. (10) and the linearity of the expected-value operator, which allows the amplitude-variation factor α_{dis} to be brought outside, it follows that

$$\alpha_{\mathrm{dis}}^2 \Phi_{vv}(K_x, k_z) = \Phi_{vv,\mathrm{dis}}(K_x, k_z), \quad (13)$$

the expected value of the magnitude squared of $\hat{v}_R(K_x, k_z)$ being the upstream turbulence spectrum $\Phi_{vv}(K_x, k_y)$. This equation indicates that substituting the undistorted turbulence spectrum with an altered one to account for the effects of turbulence distortion introduces an increase in the energy content of the turbulence term in input. This variation is due to the distortion of the energy-containing scales in the stagnation region and is not encompassed in the original formulation of Amiet's model, which indeed overestimates the radiated noise by a constant offset across the entire frequency range compared to FWH. A modification of the turbulence term without accounting for this mechanism thus yields a noise prediction corresponding to the interaction of an undistorted perturbation featuring increased amplitude with the aerodynamic surface.

The validity of this discussion also holds for the simplified formulation of Amiet's model [Eq. (A12)], implemented in the present study, where $\Theta_{vv}(\omega)$ and $l_z(\omega)$ are used in place of the wavenumber spectrum. Indeed, in the case of large airfoil spans, it is shown that

$$\Phi_{vv}(K_x, 0) = \frac{U_\infty}{\pi} \Theta_{vv}(\omega) l_z(\omega) \quad (14)$$

since the dependency on k_z of both the aeroacoustic transfer function and the wavenumber upwash-velocity spectrum becomes negligible.

Amiet's analytical procedure can be resumed from Eq. (12), which leads to Eq. (A6). This relates the cross-PSD of the surface pressure $S_{QQ}(x_1, x_2, \eta, \omega)$ to the wavenumber spectrum $\Phi_{vv}(K_x, k_z)$ via the transfer function $g(x, K_x, k_z)$. Taking into account Eqs. (13) and (14), through Eqs. (A9) and (A10), the following formulation for a distortion-corrected equation of Amiet's model is derived

$$S_{pp}(x, y, 0, \omega) = \left(\frac{\omega y \rho_\infty c}{2 c_\infty \sigma_0^2} \right)^2 \pi U_\infty \frac{L}{2} |\mathcal{L}_{\mathrm{dis}}(\boldsymbol{x}, K_x, 0)|^2 \Theta_{vv,\mathrm{dis}}(\omega) l_z(\omega),$$

$$(15)$$

with $\mathcal{L}_{\mathrm{dis}}$ indicating the corrected aeroacoustic transfer function defined to account for the increase in the gust amplitude due to the turbulence distortion at the stagnation region, whose expression is

$$\mathcal{L}_{\mathrm{dis}}(x, K_x, k_z) = \frac{1}{\alpha_{\mathrm{dis}}} \mathcal{L}(x, K_x, k_z)$$

$$= \int_{-L/2}^{L/2} \frac{1}{\alpha_{\mathrm{dis}}} g(x_0, K_x, k_z) e^{-i\omega x_0 (M - x/\sigma)/c_\infty \beta^2} \, dx_0. \quad (16)$$

Indeed, considering the factor α_{dis} as a scaling coefficient for the aeroacoustic transfer function is justified by the fact that the pressure jump on the airfoil surface, which produces the noise radiation, is caused by the altered velocity field in the stagnation region, as shown in Sec. IV B. Therefore, the local turbulence characteristics, described by the distorted spectrum sampled in that region, should be considered as they are, and the aerodynamic and acoustic response of the airfoil should be scaled accordingly as a consequence of incorporating the altered turbulence conditions. This strategy, which allows the gust amplitude in $g(x, k_x, k_z)$ to be scaled, is consistent with the approach proposed by Christophe[39] and De Santana et al.,[40] which is based on the modification of the von Kármán model considering a different decay slope of the upwash velocity spectrum and imposing the conservation of the turbulent kinetic energy.

A straightforward approach to model the energy variation with respect to upstream conditions, owing to the same assumption of large-scale turbulence interacting with the aerodynamic body, is by using the RDT analytical expressions for the asymptotic case $L_x/a \gg 1$ to evaluate the evolution of the root mean square of the velocity components along the stagnation streamline. The outcome of this quasi-steady calculation reads[31]

$$\sqrt{\overline{u'^2}} = \sqrt{\overline{u'^2_\infty}} \left(1 - \frac{1}{\left(1 - \frac{x}{a} \right)^2} \right), \quad (17)$$

$$\sqrt{\overline{v'^2}} = \sqrt{\overline{v'^2_\infty}} \left(1 + \frac{1}{\left(1 - \frac{x}{a} \right)^2} \right). \quad (18)$$

The trends of the two velocity components as a function of the characteristic dimension of the body are valid close to the stagnation point.[73] While the asymptotic analysis confirms the results discussed in Fig. 8, the root mean square of the undistorted upwash component near the body surface is amplified by a factor 2. Consequently, since the upwash velocity spectrum is sampled in the immediate vicinity of the surface, the amplitude-scaling factor α_{dis} is taken equal to 2.

It is important to stress that, in the case of thicker aerodynamic surfaces, the quasi-steady approach may no longer be representative of the acoustic response of the airfoil, leading to deviations of the gust-amplitude variation along the stagnation streamline from the large-scale behavior predicted by the linearized theory.

F. Distortion-corrected leading-edge noise prediction

As explained in Sec. IV A, the assumption of large-scale turbulence can be considered valid for the two airfoils under investigation. This means that the corrected expression of the model of Eq. (15), using the altered aeroacoustic transfer function $\mathcal{L}_{\mathrm{dis}}$ and the turbulence spectrum sampled as close as possible to the leading edge Θ_{dis}, can be applied and used to draw a comparison with the results of the FWH analogy.
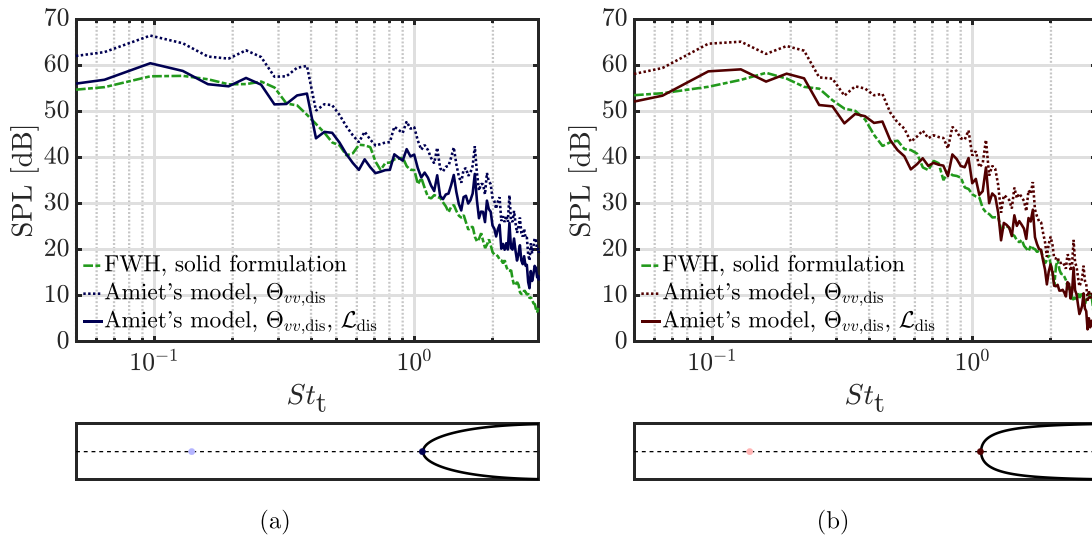
FIG. 21. Sound pressure level in the far-field calculated for an observer placed at R = 1.2 m and $\theta = \pi/2$, with the angular position computed with respect to the downstream direction, for (a) NACA 0012 and (b) NACA 0012–103. Amiet's model implementations using spectra sampled in the distorted region of the flow field $\Theta_{vv,\text{dis}}$ and the one also with the corrected transfer function $\mathcal{L}_{\text{dis}}$ are compared to the calculation provided by the FWH analogy. The reference pressure used to calculate the SPL is 2×10^{-5} Pa.

The outcomes of the above analysis are shown in terms of SPL, PWL, and far-field noise directivity patterns in Figs. 21, 22, and 23, respectively. For the latter investigation, two different frequency ranges of integration are selected: a low-frequency range $St_\text{t} = [0.15, 0.35]$ and a high-frequency one $St_\text{t} = [0.35, 1.5]$, i.e., the part of the spectrum where the noise levels are correctly estimated by the canonical application of Amiet's model and that where they are overestimated because of the wrong prediction of the spectrum decay slope.

The results of the SPL and the PWL show that this distortion-corrected formulation of Amiet's model leads to an overall good

agreement with the noise prediction yielded by the FWH analogy in terms of high-frequency decay slope and noise levels, demonstrating that the proposed approach correctly encompasses the physical mechanisms that are responsible for leading-edge noise generation. The necessity to account for a gust amplitude correction in the aeroacoustic transfer function is also confirmed by the directivity patterns. Indeed, in the low-frequency range for both airfoils [Figs. 23(a) and 23(b)], a constant overestimation is found for the application of Amiet's model using only the spectrum sampled close to the stagnation point as input. Also, in the high-frequency range, a similar trend is found for NACA
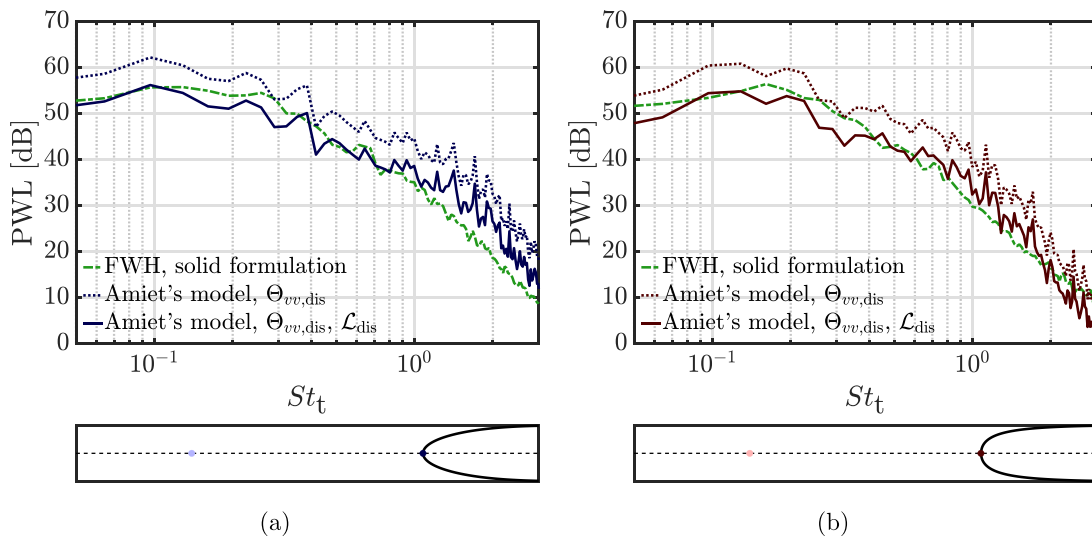

FIG. 22. Sound power level in the far-field for (a) NACA 0012 and (b) NACA 0012-103. Amiet's model implementations using spectra sampled in the distorted region of the flow field $\Theta_{vv,\text{dis}}$ and the one also with the corrected transfer function $\mathcal{L}_{\text{dis}}$ are compared to the calculation provided by the FWH analogy. The reference power used to calculate the PWL is 10^{-12} W.
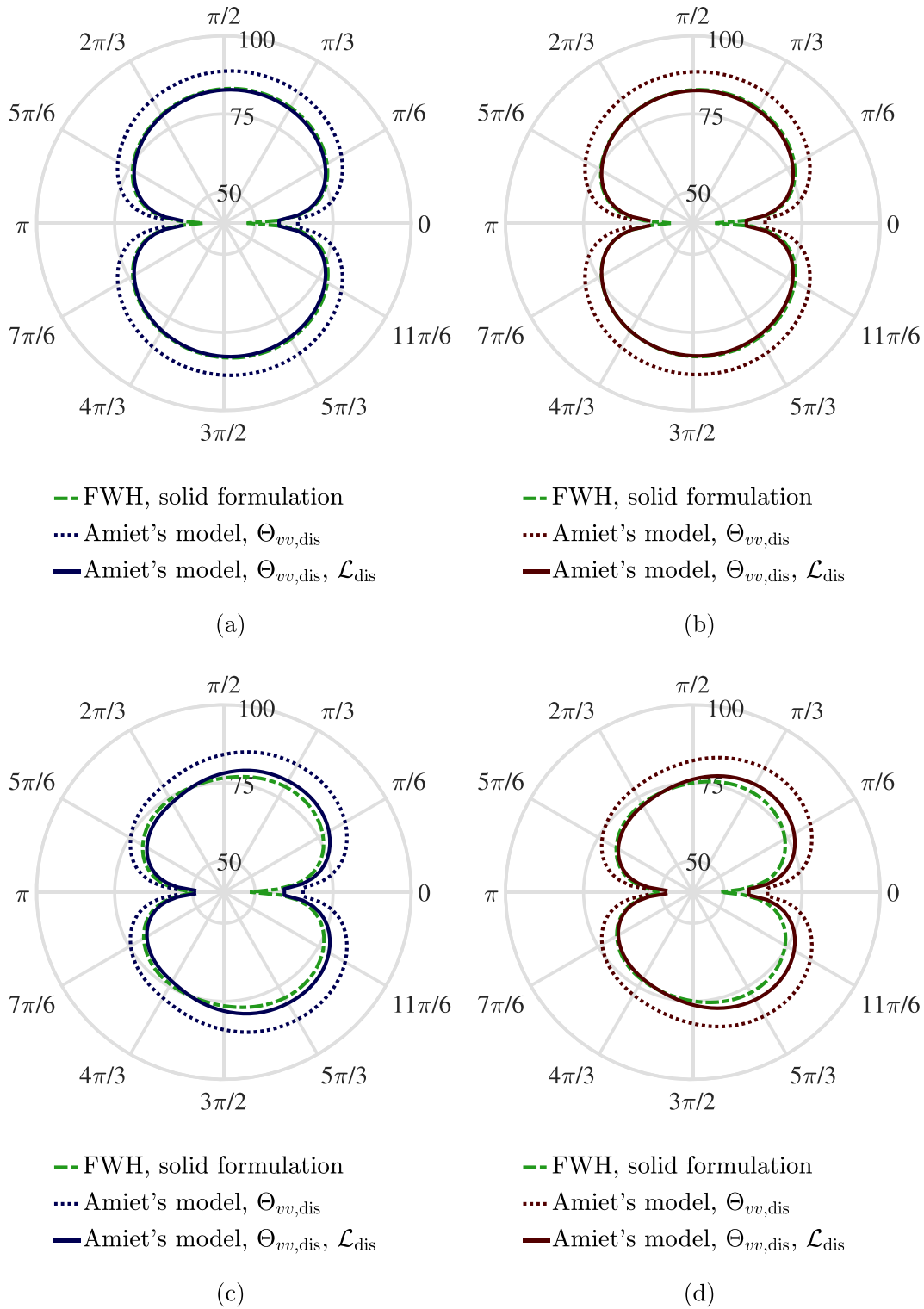
(a)

(b)

(c)

(d)

FIG. 23. Far-field noise directivity patterns in the low-frequency range $St_t = [0.15, 0.35]$ for (a) NACA 0012 and (b) NACA 0012-103 and in the high-frequency range $St_t = [0.35, 1.5]$ for (c) NACA 0012 and (d) NACA 0012-103. Amiet's model implementations using the distorted spectrum as input with and without the corrected transfer function are compared with the FWH results.

0012 and NACA 0012-103, as reported in Figs. 23(c) and 23(d), respectively. Once the correction of the transfer function is included in the formulation, a good agreement is obtained with the numerical simulations for both airfoils in the two considered frequency ranges, although a slight discrepancy is still present in the range $-\pi/3 < \theta < \pi/3$.

The implementation of this correction proves that modifying the term describing the turbulence characteristics in Amiet's model allows the distortion effects due to the realistic airfoil geometry to be accounted for in the turbulence term. The physical modeling of the noise generation is thus enhanced without requiring significant modifications in the analytical formulation of the airfoil acoustic response, at least for $L_x/a > 1$. Indeed, a correct estimation of the noise levels can be achieved through the flat-plate-based formulation of the aeroacoustic transfer function, which must be scaled accordingly to consider the effects of the altered perturbation, associated in turn with the increase in the energy content of the distorted upwash velocity component in the stagnation region.

V. CONCLUSIONS

A numerical investigation is carried out to enhance the accuracy of low-fidelity methods for predicting leading-edge noise. The characteristics of turbulence distortion are analyzed with a focus on the airfoil-geometry effects. Two airfoils, i.e., NACA 0012 and NACA 0012-103, having equal thickness but different leading-edge shapes, are considered in the interaction with grid-generated turbulence to assess the role of the leading-edge curvature on the noise-production efficiency.

The analysis of the velocity field in the vicinity of the stagnation point has excluded any dependence on the leading-edge geometrical characteristics of the extension of the region where the effects of turbulence distortion are detected, challenging, in particular, the relevance of the leading-edge radius in the definition of the distortion mechanisms. These correspond to a progressive alteration of the turbulence velocity spectra as the stagnation point is approached. Notably, an exponential decay of the upwash velocity component spectrum in the high-frequency range is observed at very small distances from the leading edge, consistently with the analytical findings of the linearized theory of Hunt.[31]

This same exponential decay seen for the turbulent velocity also characterizes the high-frequency behavior of surface-pressure spectra near the stagnation point, suggesting that noise is produced by a pressure distribution induced by the distorted velocity field in the vicinity of the leading edge. In addition to this, the noise-generation efficiency, quantified in terms of surface-pressure fluctuations, is shown to be related to airfoil curvature by means of the intensity of the pressure gradient along the leading edge. Indeed, the arc length l_{dis} extending from the stagnation point to the position of maximum curvature variation, which corresponds to the space available for the turbulent structures to accelerate along the airfoil leading edge, is found to be the geometrical parameter dictating the turbulence-distortion mechanism. As a result, the low- and high-frequency distortion behaviors observed in the analysis of the distorted turbulence spectra are univocally defined by using a Strouhal number calculated with respect to this characteristic length. This finding legitimates the extension of the results of the rapid distortion theory to realistic geometries. Further investigations in future work involving additional airfoils and loading configurations would be valuable.

The effects of turbulence distortion on the noise prediction are assessed by using as input in Amiet's model an upwash velocity spectrum acquired very close to the stagnation point. With respect to the canonical implementation of the model, the trend and, particularly, the decay slope are correctly predicted in the whole frequency range of interest, but a constant overestimation in the SPL and PWL is obtained throughout the spectrum. Such a deviation is caused by the higher amplitude of the distorted gust, related to the increase in the root mean square of the upwash velocity component in the stagnation region, which is not taken into account in the flat-plate-based formulation employed for the transfer function.

The aforementioned overestimation is not retrieved for the alternative formulation of Amiet's model computing far-field noise directly from the unsteady-pressure distribution on the airfoil surface, which does not employ a transfer function to relate the airfoil loading to the incoming turbulence. The impact of the turbulence distortion on the airfoil aerodynamic and acoustic response, i.e., the aeroacoustic transfer function, must be included to enhance the accuracy of the model in the case of thick airfoils. Indeed, the transfer function can be corrected by accounting for the gust-amplitude variation in the immediate vicinity of the airfoil leading edge with respect to upstream undistorted conditions. In the assumption of large-scale turbulence, which is considered valid in the case of the two airfoils under investigation, this variation can be modeled using the analytical trends of the root mean square of the velocity component predicted by the linearized theory. A corrected Amiet's model expression can be, hence, formulated and compared to the prediction provided by the FWH analogy. The overall good agreement obtained in terms of PWL and directivity patterns of the far-field noise proves that both physical mechanisms and their consequent analytical modeling are correctly identified in the present methodology.

Further advancements are still required in the correction of the surface acoustic response to generalize the above results to cases characterized by smaller values of L_x/a. Indeed, the modification of the transfer function implemented in the present work is valid in the asymptotic case of very large turbulence, meaning that a different formulation will likely be necessary when this condition does not hold, i.e., for a ratio L_x/a close to 1. However, the proposed approach suggests a promising development for the characterization of the airfoil-geometry effects in low-fidelity noise-prediction methods by proving that, for $L_x/a > 1$, the airfoil-geometry effects are fully encompassed by modifying the input term describing the turbulence characteristics. This conclusion entails the evaluation of the frequency spectrum of the upwash turbulent velocity in the immediate vicinity of the surface and, in turn, allows the high-frequency decay characterizing the surface-pressure spectra at the leading edge to be correctly captured.

The results of this study thus identify an improved and more robust methodology for the development of corrections aiming at the enhancement of Amiet's model through the description of turbulence-distortion effects. The paper has indeed shown that the alteration of the turbulence spectrum and the resulting effects on the aerodynamic and acoustic response shall be calculated at the stagnation point, overcoming the necessity of identifying a sampling position that is representative of the distorted turbulence characteristics, as currently proposed in the literature. Indeed, the closer to the stagnation point the upwash velocity spectrum is considered, the more accurate the modeling of the distortion effects on the leading-edge noise generation

will be. For instance, under the RDT assumptions, the solution of the linearized theory has already proven to accurately describe the changes experienced by a turbulent inflow that interacts with an airfoil by only taking the turbulence intensity and integral length scale of the incoming flow and the characteristic dimension of the body, i.e., its distortion length, as inputs.[74] In this context, no direct measurement or high-fidelity simulation would be required to assess the alteration of the flow field in the stagnation region, which could be predicted knowing the upstream, undistorted turbulence characteristics and the airfoil geometrical features.

In conclusion, the enhanced understanding gained in this paper paves the way for a semi-analytical method that extends the applicability of Amiet's model and constitutes a significant step forward in improving the accuracy of the leading-edge noise-prediction methods.

ACKNOWLEDGMENTS

AUTHOR DECLARATIONS
Conflict of Interest

The authors have no conflicts to disclose.

Author Contributions

Andrea Piccolo: Conceptualization (equal); Data curation (lead); Formal analysis (lead); Investigation (lead); Methodology (equal); Software (lead); Validation (lead); Visualization (lead); Writing – original draft (lead). **Riccardo Zamponi:** Conceptualization (equal); Formal analysis (supporting); Investigation (supporting); Methodology (equal); Supervision (equal); Writing – original draft (supporting). **Francesco Avallone:** Funding acquisition (equal); Software (supporting); Supervision (equal); Writing – review & editing (equal). **Daniele Ragni:** Funding acquisition (equal); Supervision (equal); Writing – review & editing (equal).

DATA AVAILABILITY

The data that support the findings of this study are available from the corresponding author upon reasonable request.

APPENDIX A: AMIET'S MODEL FOR LEADING-EDGE NOISE PREDICTION

A brief summary of Amiet's theory is provided hereafter. The notation used is consistent with that employed by Amiet,[2] but the axes (and consequently the notation for the velocity components) are changed to be consistent with the previously defined reference system (see Sec. II B). The model relies upon two simplifying hypotheses: the turbulence is supposed to be *frozen* while convecting and impinging on the leading edge, and the blade is considered to be an infinitely-thin flat plate of chord c and with large span L, thus neglecting the effects of thickness, camber, and angle of attack. These hypotheses allow the incident gust, with which the flat plate is interacting, to be modeled as a two-dimensional upwash velocity gust with amplitude v_0 and transverse wavenumbers k_x and k_z,

$$v(x,z) = v_0 e^{i[k_x(U_\infty t - x) - k_z z]}, \tag{A1}$$

U_∞ being the free-stream velocity. The pressure jump across the flat plate will be, hence, expressed as

$$\Delta p(x,z,t) = \pi \rho_\infty U_\infty c v_0 g(x, k_x, k_z) e^{i(k_z z - k_x U_\infty t)}, \tag{A2}$$

where $g(x, k_x, k_z)$ is the transfer function between the turbulent velocity and pressure jump, and ρ_∞ is the density. The pressure jump due to all the wavenumber components will hence be indicated by

$$\Delta p(x,z,t) = 2\pi \rho_\infty U_\infty \int\int_\infty^\infty \hat{v}_R(k_x,k_z) g(x,k_x,k_z) e^{i(k_z z - k_x U t)} dk_x dk_z \tag{A3}$$

with

$$\hat{v}_R(k_x,k_z) = \frac{1}{(2\pi)^2} \int\int_{-R}^{R} v(x,z) e^{-i(k_x x + k_z z)}. \tag{A4}$$

The variable R, large but finite, was employed in the original formulation to prevent convergence difficulties in the integration. By performing the Fourier transform with respect to time, it follows that

$$\Delta \hat{p}(x,z,\omega) = 2\pi \rho_\infty \int_\infty^\infty \hat{v}_R(K_x,k_z) g(x,K_x,k_z) e^{i(k_z z)} dk_z, \tag{A5}$$

with $T = R/U$ and $K_x = -\omega/U_\infty$ and taking into account that

$$\lim_{T\to\infty} \int_{-T}^{T} e^{i\xi t} dt = 2\pi\delta(\xi).$$

Amiet showed that the cross-spectral density S_{QQ} of the pressure jump between two points on the surface with coordinates (x_1, z_1) and (x_2, z_2) can be expressed as a function of the two-dimensional wavenumber component $\Phi_{vv}(k_x, k_y)$ via the transfer function $g(x, k_x, k_y)$,

$$S_{QQ}(x_1, x_2, \eta, \omega) = (\pi \rho_\infty c)^2 \int_{-\infty}^{+\infty} g^\dagger(x_1, K_x, k_z) g(x_2, K_x, k_z)$$
$$\times \Phi_{vv}(K_x, k_z) e^{ik_z \eta} dk_z. \tag{A6}$$

$g^\dagger(x, k_x, k_z)$ is the complex conjugate of the transfer function $g(x, k_x, k_z)$, whereas $\eta = z_2 - z_1$ is the non-dimensionalized spanwise separation of the two points on the surface.

The cross-spectral density of the surface pressure can then be related to the far-field sound using the theory of Curle,[62] according to which the acoustic response of an airfoil can be obtained by considering a distribution of dipoles on the surface with the same strength of the force acting on the surface itself. If the far-field pressure produced by an elementary force $F(x_0, z_0, \omega) e^{i\omega t} \mathbf{k}$ acting in the point $\mathbf{x}_0 = (x_0, 0, z_0)$ is indicated with $p_1(x, y, z, \omega, x_0, z_0)$, this can be expressed as

23 January 2025 12:30:40

$$p_1(x,y,z,\omega,x_0,z_0) = \frac{i\omega z F(x_o, z_0, \omega)}{4\pi c_\infty \sigma^2} e^{i\omega\left[t + \frac{M(x-x_0)-\sigma}{c_\infty\beta^2} + \frac{xx_0 + zz_0\beta^2}{c_\infty\beta^2\sigma}\right]}, \quad (A7)$$

where M is the free-stream Mach number, and c_∞ is the speed of sound. The effects of convection are accounted for in the variable σ, whose expression is

$$\sigma = \sqrt{(x-x_0)^2 + \beta^2\left[(y-y_0)^2 + (z-z_0)^2\right]}, \quad (A8)$$

with $\beta = \sqrt{1-M^2}$ being the compressibility factor. The observer position is located at $\boldsymbol{x} = (x,y,z)$.

By integrating the cross-spectral density of the pressure jump on the whole surface, the loading acting on the airfoil is related to the far-field acoustic pressure S_{pp} through

$$S_{pp}(\boldsymbol{x},\omega) = \left(\frac{\omega z}{4\pi c_0\sigma^2}\right)^2 \iiiint S_{QQ}(x_1, x_2, \eta, \omega)$$
$$\times e^{\frac{i\omega}{c_0}\left[\beta^{-2}(x_1-x_2)\left(M-\frac{x}{\sigma}\right) + \frac{\eta\eta}{\sigma}\right]} dx_1 dx_2 dy_1 dy_2. \quad (A9)$$

By substituting Eq. (A6) in Eq. (A9), the far-field acoustic pressure as a function of incoming turbulence spectrum can be expressed as

$$S_{pp}(\boldsymbol{x},\omega) = \left(\frac{\omega y\rho_\infty c}{2c_\infty\sigma^2}\right)^2 \pi U_\infty \frac{L}{2}$$
$$\times \int_{-\infty}^{+\infty} \frac{\sin^2\left[\frac{L}{2}\left(k_z + \frac{\omega z}{c_\infty\sigma}\right)\right]}{\left(k_z + \frac{\omega z}{c_\infty\sigma}\right)^2 \pi \frac{L}{2}}$$
$$\times |\mathcal{L}(\boldsymbol{x}, K_x, k_z)|^2 \Phi_{vv}(K_x, k_z) dk_z. \quad (A10)$$

$\mathcal{L}$ is the total aeroacoustic transfer function, retrieved from the transfer function $g(x, K_x, k_z)$ through

$$\mathcal{L}(x, K_x, k_z) = \int_{-L/2}^{L/2} g(x_0, K_x, k_z) e^{-i\omega x_0(M-x/\sigma)/c_\infty\beta^2} dx_0. \quad (A11)$$

In the case of a flat plate, this function can be calculated analytically, while, for thicker airfoils, numerical methodologies must be carried out.[75] The formulation employed in this study implements the derivation of de Santana *et al.*[40] and de Santana *et al.*,[76] detailed in Appendix B, which derives the aeroacoustic transfer function as the sum of the leading-edge term $\mathcal{L}_1$ and trailing-edge term $\mathcal{L}_2$. These two contributions express the noise emitted by the scattering of the incoming turbulence at the leading edge and the back-scattering correction[77] of that incident field at the trailing edge, respectively.

A simplified formulation of Amiet's model is implemented in the present work. Indeed, Eq. (A10) can be simplified by assuming a large span and considering a listener at the midspan plane of the airfoil

$$S_{pp}(x,y,0,\omega) = \left(\frac{\omega y\rho_\infty c}{2c_\infty\sigma_0^2}\right)^2 \pi U_\infty \frac{L}{2} |\mathcal{L}(\boldsymbol{x}, K_x, 0)|^2 \Theta_{vv}(\omega) l_z(\omega), \quad (A12)$$

where Θ_{vv} is the PSD of the upwash velocity fluctuations, and l_z is the spanwise coherence length of the velocity fluctuations impinging on the airfoil. This is calculated considering the spanwise

distribution of the upwash velocity component in the same positions where the frequency spectrum is sampled using the following expression[41,42,77]

$$l_z(\omega) = \int_0^\infty \sqrt{\gamma_{v'v'}^2(\omega, z)} dz, \quad (A13)$$

with γ^2 being the magnitude square coherence defined as

$$\gamma_{s_1 s_2}^2(\omega) = \frac{|\Theta_{s_1 s_2}(\omega)|^2}{\Theta_{s_1 s_1}(\omega)\Theta_{s_2 s_2}(\omega)}, \quad (A14)$$

s_1 being a reference time signal and s_2 a generic one, $\Theta_{s_1 s_1}$ and $\Theta_{s_2 s_2}$ the respective power spectral densities and $\Theta_{s_1 s_2}$ the cross-spectral density of the two variables.

APPENDIX B: AEROACOUSTIC TRANSFER FUNCTION

The aeroacoustic transfer function $\mathcal{L}$ is implemented following de Santana *et al.*[40] and de Santana *et al.*,[76] where it is obtained as the sum of the two contributions $\mathcal{L}_1$ and $\mathcal{L}_2$. The two terms are retrieved by calculating the pressure distribution induced by the sinusoidal perturbation, whose expressions are

$$p_1(x,0,z,t) = \rho_\infty U_\infty v_0 \frac{e^{-i\pi/4}\left(\frac{k_x c}{2\beta^2} - \kappa\right)}{\sqrt{\pi\left(\frac{k_x c}{2\beta^2} - \kappa\right)\left[\left(\frac{k_x c}{2}\right)^2 + \left(\frac{k_z c}{2}\right)^2\right]\frac{2x}{c}}}$$
$$\times e^{i\left(\omega t - \left[\left(\frac{k_x c}{2\beta^2} - \kappa\right)/b - k_x\right]x - k_z z\right)} \quad (B1)$$

for the leading-edge term and

$$p_2(x,0,z,t) \simeq -\rho_\infty U_\infty v_0 \frac{1}{\sqrt{2\pi\left[\left(\frac{k_x c}{2}\right)^2 + \beta^2\kappa\right]}}$$
$$\times \left[1 - (1+i)E^*\left(2\kappa\left(2 - \frac{2x}{c}\right)\right)\right]$$
$$\times e^{i\left[\left(\frac{k_x c}{2\beta^2}M^2\right)\frac{2x}{c} - \pi/4 + \omega t - k_z z\right]} \quad (B2)$$

for the trailing-edge one, with $\kappa^2 = \mu^2 - k_z c/(2\beta^2)$, and $\mu = k_x cM/(2\beta^2)$. The function $E^*(x)$ is a combination of the Fresnel's integrals C_2 and S_2 with the following expression

$$E^*(x) = \int_0^x \frac{e^{-it}}{\sqrt{2\pi t}} dt = C_2(x) - iS_2(x), \quad (B3)$$

with

$$C_2(x) = \frac{1}{\sqrt{2\pi}} \int_0^x \frac{\cos(t)}{\sqrt{t}} dt; \quad (B4)$$

and

$$S_2(x) = \frac{1}{\sqrt{2\pi}} \int_0^x \frac{\sin(t)}{\sqrt{t}} dt. \quad (B5)$$

These expressions, valid in the case of supercritical gust ($\kappa^2 > 0$), are then substituted into $g(x, k_x, k_z)$, which is retrieved by rearranging Eq. (A2) as

$$g(x, k_x, k_z) = \frac{\Delta p(x, z, t) e^{i(k_x U_\infty t - k_z z)}}{\pi \rho_0 U_\infty c v_0}. \quad (B6)$$

$\mathcal{L}_1$ and $\mathcal{L}_2$ are then obtained by substituting the resulting expressions into Eq. (A11), yielding

$$\mathcal{L}_1(x, y, z, k_x, k_z) = \frac{1}{\pi} \sqrt{\frac{2}{\left(\frac{k_x c}{2} + \beta^2 \kappa\right) \theta_1}} E^*(2\theta_1) e^{i\theta_2}, \quad (B7)$$

and

$$\mathcal{L}_2(x, y, z, k_x, k_z)$$
$$\simeq \frac{e^{i\theta_2}}{\pi \theta_1 \sqrt{2\pi \left(\frac{k_x c}{2} + \beta^2 \kappa\right)}}$$
$$\times \left\{ i(1 - e^{-2i\theta_1}) + (1 - i) \left[E^*(4\kappa) - \sqrt{\frac{2\kappa}{\theta_3}} e^{-2i\theta_1} E^*(2\theta_3) \right] \right\}, \quad (B8)$$

where $\theta_1 = \kappa - \mu x/\sigma_0$, $\theta_2 = \mu(M - x/\sigma_0) - \pi/4$, $\theta_3 = \kappa + \mu x/\sigma_0$.

APPENDIX C: TURBULENCE CHARACTERIZATION

The characteristics of the grid-generated turbulence at the exit of the open-jet wind tunnel are further investigated by assessing the flow anisotropy and homogeneity. The analysis of the turbulence characteristics at the nozzle exit, carried out in terms of turbulence intensity of the velocity components and turbulence spectra, has highlighted a slight anisotropy of the flow. More specifically, the fluctuation of the upwash velocity component appears to be larger than that of the streamwise velocity component. This is consistent with the known behavior of turbulent structures experiencing a distortion caused by a contraction, which leads indeed to an increase in vorticity along the axis of the contraction and a consequent decrease in the two normal directions. This causes the energy to redistribute from the streamwise to the upwash and spanwise velocity fluctuations.[8,33,78,79] As shown by Batchelor and Proudman,[33] the energy redistribution is proportional to the contraction ratio, which is related to the section variation in the final part of the nozzle. Considering the dimensions of the grid-generating turbulence and the nozzle exit section, the contraction is equal to 4.16. This value is significantly larger than those commonly employed in the literature to adjust the flow anisotropy downstream of a grid, which are on

the order of 1,[78–80] and explains the higher fluctuation observed for the upwash velocity component with respect to the isotropic state observed in Sec. III B.

The variations of the ratio between the root mean square of the velocity-components fluctuations in the streamwise direction, shown in Fig. 24, are a further confirmation of the hypothesis formed above. These trends, showing the evolution of the flow from $x/c = -1.5$ to 0, indicate that the upwash velocity component and the spanwise velocity one feature increasingly similar fluctuations, larger than those characterizing the streamwise velocity component. An ancillary x axis is reported to indicate the variation of the ratios with respect to the distance from the turbulence-generating grid, expressed in terms of the mesh size W.

However, this analysis only provides information on the isotropy of the energy-containing scales. As emerged from the study of the turbulence frequency spectrum of the upwash velocity component [Fig. 5(b)], the anisotropy characterizes mostly the large scales of turbulence. The following relations for the velocity derivatives are more representative of the behavior and characteristics of small-scale structures[80]

$$\overline{\left(\frac{\partial u'}{\partial z}\right)^2} = 2 \overline{\left(\frac{\partial u'}{\partial x}\right)^2}, \quad (C1a)$$

$$\overline{\left(\frac{\partial w'}{\partial x}\right)^2} = 2 \overline{\left(\frac{\partial u'}{\partial x}\right)^2}, \quad (C1b)$$

$$-\overline{\left(\frac{\partial u'}{\partial z}\right)\left(\frac{\partial w'}{\partial x}\right)} = \frac{1}{2} \overline{\left(\frac{\partial u'}{\partial x}\right)^2}. \quad (C1c)$$

Figure 25 reports these relations in the form of ratios with respect to $\overline{\left(\frac{\partial u'}{\partial x}\right)^2}$. Satisfactory isotropy levels are observed as the flow develops in the streamwise direction, with the curves of Eqs. (C1a) and (C1b) overlapping with the asymptote at 2 and that of Eq. (C1c) very close to 1/2.

Skewness S_k and kurtosis K_r of the streamwise velocity component along the stagnation streamline have also been investigated to assess the similarity of the probability density function (PDF) of this fluctuating velocity component to a Gaussian distribution.[81,82] The results are reported in Fig. 26. The skewness and kurtosis of the upwash and spanwise velocity components are omitted in this study since they show very similar behavior to that of the streamwise velocity. Both S_k and K_r stay within the ranges specified in the literature to indicate the isotropy of the flow, equal to $[-1, 1]$ for the skewness and to $[2, 4]$ for the kurtosis.
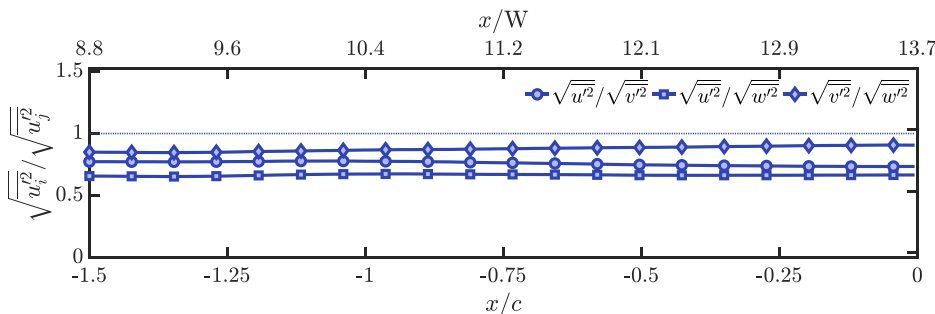

FIG. 24. Ratios of the root mean square of the three velocity components along the stagnation streamline between $x/c = -1.5$ and 0.
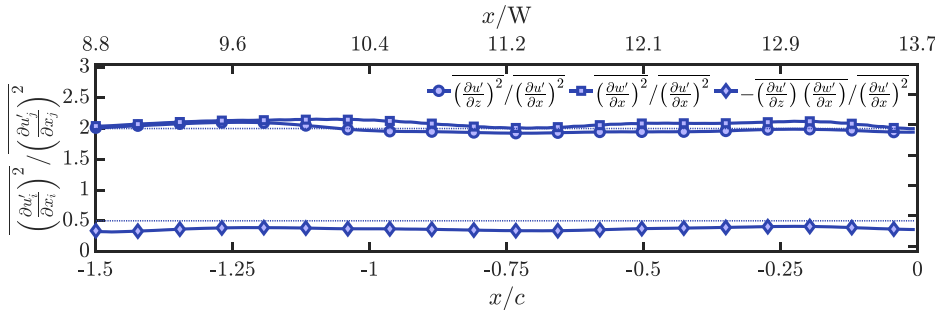
FIG. 25. Ratios of the second-order velocity derivative moments of Eq. (C1) along the stagnation streamline between $x/c = -1.5$ and 0.
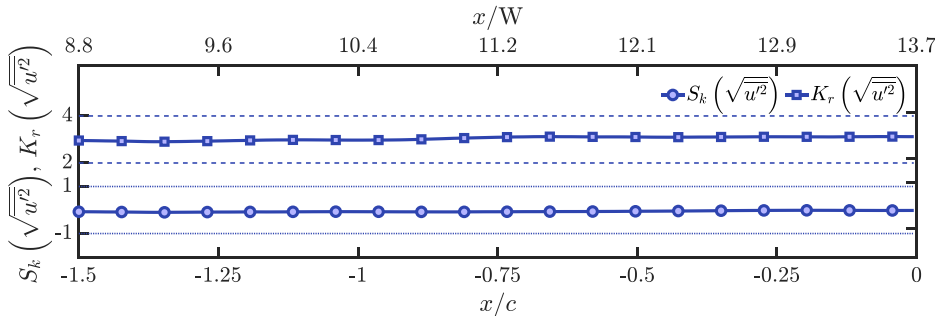

FIG. 26. Skewness and kurtosis of the streamwise velocity component along the stagnation streamline between $x/c = -1.5$ and 0.

Further information on the turbulent flow after the distortion occurring in the final part of the nozzle is obtained by analyzing the anisotropy invariant map, also known as Lumley triangle.[83–85] This technique provides insight into the return to isotropy of grid-generated turbulence by using the second and third invariants of the anisotropy tensor, whose non-dimensional form is

$$b_{ij} = \frac{\overline{u_i' u_j'}}{2k_t} - \frac{1}{3}\delta_{ij}, \quad (C2)$$

with δ_{ij} being the Kronecker delta and $k_t = \overline{u_i' u_i'}/2$ the turbulent kinetic energy, related to the trace of the Reynolds stress tensor. For incompressible flows, the invariants I, II, and III are retrieved by the anisotropy tensor terms through the expressions

$$\text{I} = b_{kk} = 0, \quad (C3)$$

$$\text{II} = \frac{b_{ij}b_{ji}}{2}, \quad (C4)$$

$$\text{III} = \frac{b_{ij}b_{jn}b_{ni}}{3}, \quad (C5)$$

which are used to create a coordinate system (III), (II).[86] The range of invariants, and hence the possible states of turbulence, must fall within the boundaries shown in Fig. 27: one-dimensional turbulence (III = 2/27 and II = 1/3) in the right-hand corner, two-component axisymmetric turbulence (III = −1/108 and II = 1/12) in the left-hand corner, and isotropic turbulence (III = 0 and II = 0) at the origin of the plot. Turbulence in the left region has one component smaller than the other two, as in the case of an axisymmetric contraction,[86] and is defined as "disk-like" or "pancake-shaped" turbulence. In the right region, turbulence has one component of the turbulent kinetic energy higher than the other two, as occurs for

axisymmetric expansion, and is defined as "rod-like" or "cigar-shaped".[85] The anisotropy tensor invariants are calculated at six positions equally spaced along the streamwise direction between $x/c = -1.5$ and 0 in the midspan plane ($y = 0$, $z = 0$), thus yielding six points in the invariant map. The results, reported in Fig. 27, indicate that turbulence slightly tends to the left-hand side of the triangle, consistently with the distortion mechanism occurring in a converging section, but is close to the isotropic condition.

Finally, flow homogeneity at the nozzle exit is assessed by analyzing the spanwise distribution of the time average and the root mean square of the three velocity components. These distributions
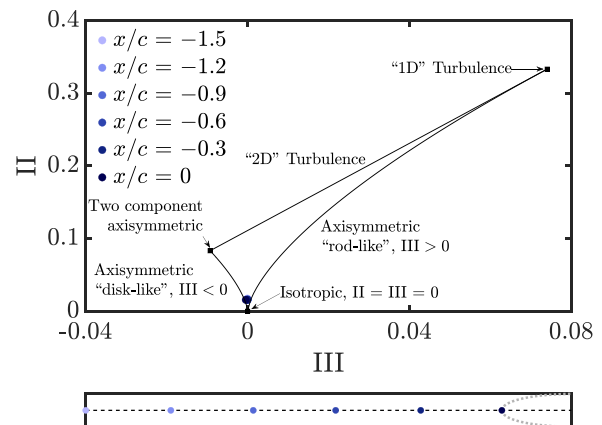

FIG. 27. Anisotropy invariant map for six positions along the streamwise direction (indicated in the plot) at $y = 0$ and $z = 0$. The position where the airfoil will be placed is reported as a reference in the plot below.
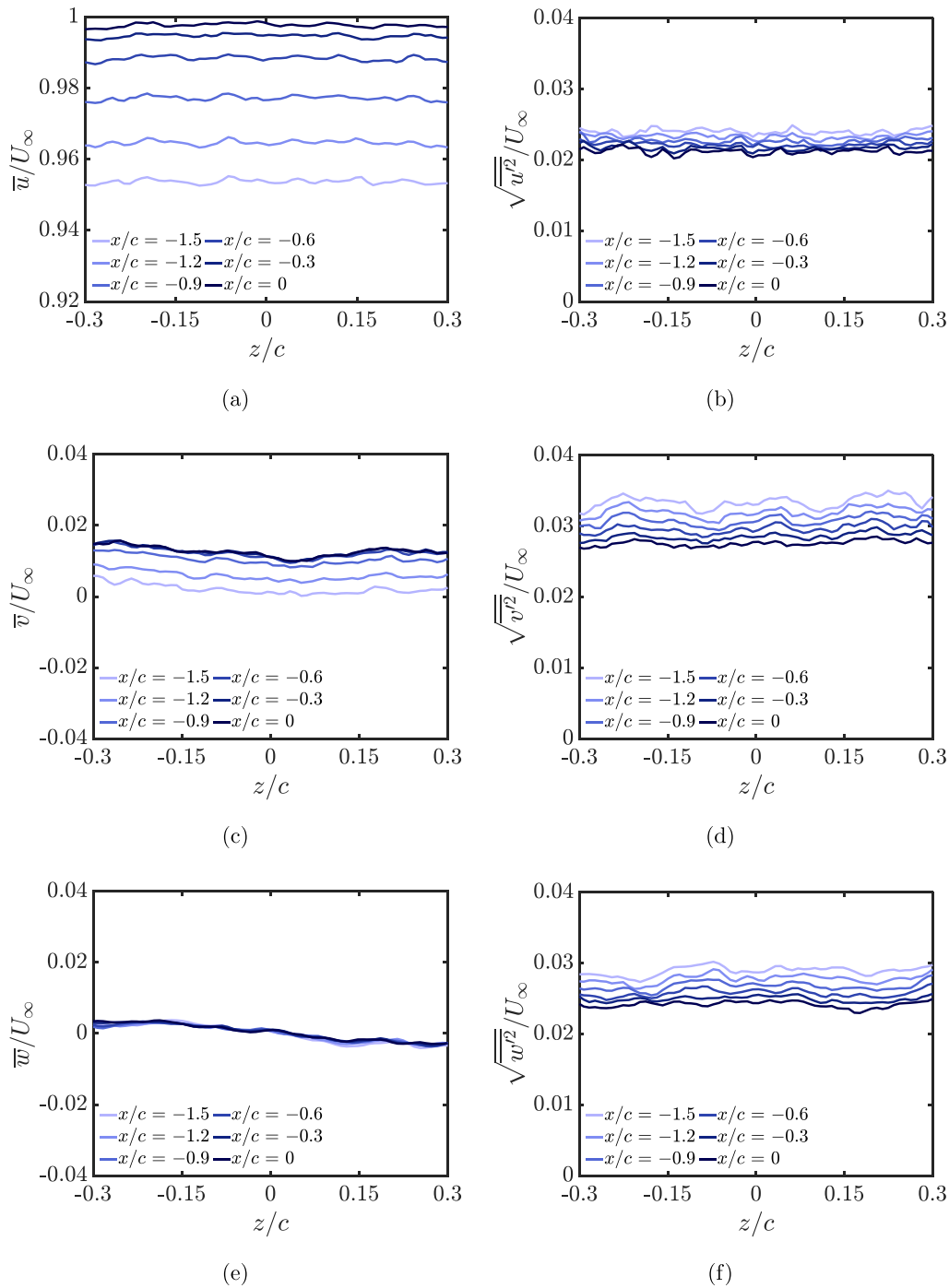
FIG. 28. Spanwise distribution of the (a), (c), (e) time-average and (b), (d), (f) root mean square of the three velocity components at six different positions along the stagnation streamline between $x/c = -1.5$ and 0.

are shown from $z/c = -0.36$ to 0.36 in Figs. 28(a), 28(c), 28(e), and Figs. 28(b), 28(d), 28(f), respectively. The time-averaged values of the streamwise velocity component show a progressive acceleration at the exit of the nozzle, as expected. For the upwash velocity component, whose distribution can be considered homogeneous in the spanwise direction, a small increase below 2% of the free-stream streamwise velocity is found. The spanwise velocity component remains equal to zero.

As regards the spanwise distribution of the root mean square of the velocity fluctuations, all three components exhibit a progressive decrease in the streamwise direction. At the upstream locations inside the nozzle, a spanwise periodicity still characterizes the distributions of the upwash velocity component and, mildly, the spanwise one. This indicates that the coalescence of the wakes generated by the rectangular grid, whose collection constitutes the turbulent flow field,[87] is still ongoing in the last part of the nozzle. This periodic pattern reduces as the distance from the nozzle exit increases, and a homogeneous condition is reached at the most downstream position, where the airfoil is placed.

REFERENCES

[1] J. M. R. Graham, "Similarity rules for thin aerofoils in non-stationary subsonic flows," J. Fluid Mech. **43**, 753–766 (1970).

[2] R. K. Amiet, "Acoustic radiation from an airfoil in a turbulent stream," J. Sound Vib. **41**, 407–420 (1975).

[3] R. Paterson and R. Amiet, "Acoustic radiation and surface pressure characteristics of an airfoil due to incident turbulence," in *3rd Aeroacoustics Conference, Aeroacoustics Conferences* (American Institute of Aeronautics and Astronautics, 1976).

[4] R. W. Paterson and R. K. Amiet, "Noise and surface pressure response of an airfoil to incident turbulence," J. Aircraft **14**, 729–736 (1977).

[5] R. W. Paterson and R. K. Amiet, "Noise of a model helicopter rotor due to ingestion of turbulence," Technical Report No. NASA-CR-3213 (National Aeronautics and Space Administration, 1979).

[6] M. S. Howe, "Aerodynamic noise of a serrated trailing edge," J. Fluids Struct. **5**, 33–45 (1991).

[7] S. Oerlemans, "Reduction of wind turbine noise using blade trailing edge devices," in *22nd AIAA/CEAS Aeroacoustics Conference, Aeroacoustics Conferences* (American Institute of Aeronautics and Astronautics, 2016).

[8] R. K. Amiet, J. C. Simonich, and R. H. Schlinker, "Rotor noise due to atmospheric turbulence ingestion. II - Aeroacoustic results," J. Aircraft **27**, 15–22 (1990).

[9] C. Teruna, F. Avallone, D. Casalino, and D. Ragni, "Numerical investigation of leading edge noise reduction on a rod-airfoil configuration using porous materials and serrations," J. Sound Vib. **494**, 115880 (2021).

[10] S. Oerlemans, *Wind Turbine Noise: Primary Noise Sources* (MultiScience, 2011).

[11] S. Buck, S. Oerlemans, and S. Palo, "Experimental characterization of turbulent inflow noise on a full-scale wind turbine," J. Sound Vib. **385**, 219–238 (2016).

[12] O. Amoiridis, A. Zarri, R. Zamponi, Y. Pasco, G. Yakhina, J. Christophe, S. Moreau, and C. Schram, "Sound localization and quantification analysis of an automotive engine cooling module," J. Sound Vib. **517**, 116534 (2022).

[13] P. Moriarty, G. Guidati, and P. Migliore, "Recent improvement of a semi-empirical aeroacoustic prediction code for wind turbines," in *10th AIAA/CEAS Aeroacoustics Conference* (American Institute of Aeronautics and Astronautics, 2004).

[14] M. E. Goldstein and H. Atassi, "A complete second-order theory for the unsteady flow about an airfoil due to a periodic gust," J. Fluid Mech. **74**, 741–765 (1976).

[15] W. Olsen and J. Wagner, "Effect of thickness on airfoil surface noise," AIAA J. **20**, 437–439 (1982).

[16] H. Atassi, S. Subramaniam, and J. Scott, "Acoustic radiation from lifting airfoils in compressible subsonic flow," in *13th Aeroacoustics Conference, Aeroacoustics Conferences* (American Institute of Aeronautics and Astronautics, 1990).

[17] D. P. Lockard and P. J. Morris, "Radiated noise from airfoils in realistic mean flows," AIAA J. **36**, 907–914 (1998).

[18] S. A. L. Glegg and W. J. Devenport, "Unsteady loading on an airfoil of arbitrary thickness," J. Sound Vib. **319**, 1252–1270 (2009).

[19] S. A. L. Glegg and W. J. Devenport, "Panel methods for airfoils in turbulent flow," J. Sound Vib. **329**, 3709–3720 (2010).

[20] S. Oerlemans, "Wind tunnel aeroacoustic tests of six airfoils for use on small wind turbines; period of performance: August 23, 2002 through March 31, 2004," Technical Report No. NREL/SR-500–35339, 15007773 (National Renewable Energy Laboratory, 2004).

[21] A. Hall, O. Atassi, J. Gilson, R. Reba, and D. Shannon, "Effect of leading-edge thickness on high-speed airfoil-turbulence interaction noise," in *17th AIAA/CEAS Aeroacoustics Conference (32nd AIAA Aeroacoustics Conference), Aeroacoustics Conferences* (American Institute of Aeronautics and Astronautics, 2011).

[22] P. Chaitanya, J. R. Gill, S. Narayanan, P. Joseph, C. Vanderwel, X. Zhang, and B. Ganapathisubramani, "Aerofoil geometry effects on turbulence interaction noise," in *21st AIAA/CEAS Aeroacoustics Conference*, AIAA AVIATION Forum (American Institute of Aeronautics and Astronautics, 2015).

[23] W. J. Devenport, J. K. Staubs, and S. A. L. Glegg, "Sound radiation from real airfoils in turbulence," J. Sound Vib. **329**, 3470–3483 (2010).

[24] J. Gill, X. Zhang, and P. Joseph, "Symmetric airfoil geometry effects on leading edge noise," J. Acoust. Soc. Am. **134**, 2669–2680 (2013).

[25] L. Bowen, A. Celik, and M. Azarpeyvand, "A thorough experimental investigation on airfoil turbulence interaction noise," Phys. Fluids **35**, 035123 (2023).

[26] G. Guidati, R. Bareiss, S. Wagner, and R. Parchen, "Simulation and measurement of inflow-turbulence noise on airfoils," in *3rd AIAA/CEAS Aeroacoustics Conference* (American Institute of Aeronautics and Astronautics, 1997).

[27] J. Gershfeld, "Leading edge noise from thick foils in turbulent flows," J. Acoust. Soc. Am. **116**, 1416–1426 (2004).

[28] M. S. Howe, "Contributions to the theory of aerodynamic sound, with application to excess jet noise and the theory of the flute," J. Fluid Mech. **71**, 625–673 (1975).

[29] P. D. Lysak, D. E. Capone, and M. E. Jonson, "Prediction of high frequency gust response with airfoil thickness effects," J. Fluids Struct. **39**, 258–274 (2013).

[30] D. Kim, G. Lee, and C. Cheong, "Inflow broadband noise from an isolated symmetric airfoil interacting with incident turbulence," J. Fluids Struct. **55**, 428–450 (2015).

[31] J. C. R. Hunt, "A theory of turbulent flow round two-dimensional bluff bodies," J. Fluid Mech. **61**, 625–706 (1973).

[32] H. S. Ribner and M. Tucker, *Spectrum of Turbulence in a Contracting Stream* (National Advisory Committee for Aeronautics, 1953).

[33] G. K. Batchelor and I. Proudman, "The effect of rapid distortion of a fluid in turbulent motion," Q. J. Mech. Appl. Math. **7**, 83–103 (1954).

[34] L. Prandtl, "Attaining a steady air stream in wind tunnels," Report No. NACA-TM-726, 1933.

[35] G. I. Taylor, "Turbulence in a contracting stream," Z. Angew. Math. Mech. **15**, 91–96 (1935).

[36] P. Mish and W. Devenport, "An experimental investigation of unsteady surface pressure on an airfoil in turbulence—Part 1: Effects of mean loading," J. Sound Vib. **296**, 417–446 (2006).

[37] P. Mish and W. Devenport, "An experimental investigation of unsteady surface pressure on an airfoil in turbulence—Part 2: Sources and prediction of mean loading effects," J. Sound Vib. **296**, 447–460 (2006).

[38] S. Moreau and M. Roger, "Effect of angle of attack and airfoil shape on turbulence-interaction noise," in *11th AIAA/CEAS Aeroacoustics Conference* (American Institute of Aeronautics and Astronautics, 2005).

[39] J. Christophe, "Application of hybrid methods to high frequency aeroacoustics," Ph.D. thesis, Université Libre de Bruxelles, 2011.

[40] D. D. Santana, J. Christophe, C. Schram, and W. Desmet, "A Rapid Distortion Theory modified turbulence spectra for semi-analytical airfoil noise prediction," J. Sound Vib. **383**, 349–363 (2016).

[41] F. L. dos Santos, L. Botero-Bolívar, C. Venner, and L. D. Santana, "Modeling the turbulence spectrum dissipation range for leading-edge noise prediction," AIAA J. **60**, 1–12, (2022).

[42] F. L. dos Santos, L. Botero Bolivar, C. Venner, and L. De Santana, "Inflow turbulence distortion for airfoil leading-edge noise prediction for large turbulence length scales for zero-mean loading," J. Acoust. Soc. Am. **153**, 1811–1822 (2023).

[43] A. Piccolo, R. Zamponi, F. Avallone, and D. Ragni, "Turbulence-distortion analysis for leading-edge noise-prediction enhancement," in *AIAA AVIATION 2023 Forum* (American Institute of Aeronautics and Astronautics, 2023).

[44] J. E. Ffowcs Williams and D. L. Hawkings, "Sound generation by turbulence and surfaces in arbitrary motion," Philos. Trans. Roy. Soc. Lond. Ser. A, Math. Phys. Sci. **264**, 321–342 (1969).

[45]S. Succi, *The Lattice Boltzmann Equation: For Fluid Dynamics and Beyond*, Numerical Mathematics and Scientific Computation (Oxford University Press, Oxford, New York, 2001).

[46]H. Chen, S. Chen, and W. H. Matthaeus, "Recovery of the Navier-Stokes equations using a lattice-gas Boltzmann method," Phys. Rev. A **45**, R5339–R5342 (1992).

[47]P. L. Bhatnagar, E. P. Gross, and M. Krook, "A model for collision processes in gases. I. Small amplitude processes in charged and neutral one-component systems," Phys. Rev. **94**, 511–525 (1954).

[48]H. Xu and P. Sagaut, "Optimal low-dispersion low-dissipation LBM schemes for computational aeroacoustics," J. Comput. Phys. **230**, 5353 (2011).

[49]J. Meng, X.-J. Gu, and D. R. Emerson, "Analysis of non-physical slip velocity in lattice Boltzmann simulations using the bounce-back scheme," J. Comput. Sci. **28**, 476–482 (2018).

[50]D. R. Noble, S. Chen, J. G. Georgiadis, and R. O. Buckius, "A consistent hydrodynamic boundary condition for the lattice Boltzmann method," Phys. Fluids **7**, 203–209 (1995).

[51]H. Chen, P. Gopalakrishnan, and R. Zhang, "Recovery of Galilean invariance in thermal lattice Boltzmann models for arbitrary Prandtl number," arXiv:1403.2357 (2014).

[52]M. B. Reider and J. D. Sterling, "Accuracy of discrete-velocity BGK models for the simulation of the incompressible Navier-Stokes equations," Comput. Fluids **24**, 459–467 (1995).

[53]C. Teruna, "Aerodynamic noise reduction with porous materials," Ph.D. thesis, (Technische Universiteit Delft, 2022).

[54]V. Yakhot and S. Orszag, "Renormalization group analysis of turbulence. I. Basic theory," J. Sci. Comput. **1**, 3–51 (1986).

[55]V. Yakhot, S. A. Orszag, S. Thangam, T. B. Gatski, and C. G. Speziale, "Development of turbulence models for shear flows by a double expansion technique," Phys. Fluids A **4**, 1510–1520 (1992).

[56]H. Chen, S. Orszag, I. Staroselsky, and S. Succi, "Expanded analogy between Boltzmann kinetic theory of fluids and turbulence," J. Fluid Mech. **519**, 301–314 (2004).

[57]H. Chen, C. Teixeira, and K. Molvig, "Realization of fluid boundary conditions via discrete Boltzmann dynamics," Int. J. Mod. Phys. C **09**, 1281–1292 (1998).

[58]B. E. Launder and D. B. Spalding, "The numerical computation of turbulent flows," Comput. Methods Appl. Mech. Eng. **3**, 269–289 (1974).

[59]F. Farassat and G. P. Succi, "A review of propeller discrete frequency noise prediction technology with emphasis on two current methods for time domain calculations," J. Sound Vib. **71**, 399–419 (1980).

[60]G. Brès, F. Pérot, and D. Freed, "Properties of the Lattice Boltzmann Method for Acoustics," in *15th AIAA/CEAS Aeroacoustics Conference (30th AIAA Aeroacoustics Conference), Aeroacoustics Conferences* (American Institute of Aeronautics and Astronautics, 2009).

[61]D. Casalino, M. Jacob, and M. Roger, "Prediction of rod-airfoil interaction noise using the Ffowcs–Williams and Hawkings analogy," AIAA J. **71**, 182–191 (2003).

[62]N. Curle, "The influence of solid boundaries upon aerodynamic sound," Proc. Roy. Soc. Lond. Ser. A **231**, 505–514 (1955).

[63]P. E. Roach, "The generation of nearly isotropic turbulence by means of grids," Int. J. Heat Fluid Flow **8**, 82–92 (1987).

[64]I. Abbott and V. Doenhoff, *Theory of Wing Sections* (Dover Publications, 1959).

[65]S. Narayanan, P. Chaitanya, S. Haeri, P. Joseph, J. W. Kim, and C. Polacsek, "Airfoil noise reductions through leading edge serrations," Phys. Fluids **27**, 025109 (2015).

[66]S. B. Pope, *Turbulent Flows* (Cambridge University Press, 2000).

[67]S. Glegg and W. Devenport, "Turbulence and stochastic processes," in *Aeroacoustics of Low Mach Number Flows*, edited by S. Glegg and W. Devenport (Academic Press, 2017), pp. 163–184.

[68]J. C. R. Hunt, H. Kawai, S. R. Ramsey, G. Pedrizetti, and R. J. Perkins, "A review of velocity and pressure fluctuations in turbulent flows around bluff bodies," J. Wind Eng. Ind Aerodyn. **35**, 49–85 (1990).

[69]R. Zamponi, S. Satcunanathan, S. Moreau, M. Meinke, W. Schröder, and C. Schram, "Effect of porosity on Curle's dipolar sources on an aerofoil in turbulent flow," J. Sound Vib. **542**, 117353 (2023).

[70]P. Moriarty, G. Guidati, and P. Migliore, "Prediction of turbulent inflow and trailing-edge noise for wind turbines," in *11th AIAA/CEAS Aeroacoustics Conference* (American Institute of Aeronautics and Astronautics, 2005).

[71]P. A. Durbin and J. C. R. Hunt, "On surface pressure fluctuations beneath turbulent flow round bluff bodies," J. Fluid Mech. **100**, 161–184 (1980).

[72]M. J. Lighthill, "Drift," J. Fluid Mech. **1**, 31–53 (1956).

[73]R. Zamponi, S. Satcunanathan, S. Moreau, D. Ragni, M. Meinke, W. Schröder, and C. Schram, "On the role of turbulence distortion on leading-edge noise reduction by means of porosity," J. Sound Vib. **485**, 115561 (2020).

[74]R. Zamponi, S. Moreau, and C. Schram, "Rapid distortion theory of turbulent flow around a porous cylinder," J. Fluid Mech. **915**, A27 (2021).

[75]R. Miotto, W. Wolf, and L. De Santana, "Numerical computation of aeroacoustic transfer functions for realistic airfoils," J. Sound Vib. **407**, 253–270 (2017).

[76]L. De Santana, C. Schram, and W. Desmet, "Airfoil noise prediction from 2D3C PIV data," in *21st AIAA/CEAS Aeroacoustics Conference* (AIAA, 2015).

[77]M. Roger and S. Moreau, "Back-scattering correction and further extensions of Amiet's trailing-edge noise model. Part 1: Theory," J. Sound Vib. **286**, 477–506 (2005).

[78]M. Uberoi, "Effect of wind-tunnel contraction on free-stream turbulence," J. Aeronaut. Sci. **23**, 8 (1956).

[79]G. Comte-Bellot and S. Corrsin, "The use of a contraction to improve the isotropy of grid-generated turbulence," J. Fluid Mech. **25**, 657–682 (1966).

[80]P. Lavoie, L. Djenidi, and R. A. Antonia, "Effects of initial conditions in decaying turbulence generated by passive grids," J. Fluid Mech. **585**, 395–420 (2007).

[81]R. J. Hearst, "Fractal, classical, and active grid turbulence: From production to decay," Ph.D. thesis, University of Toronto, 2015.

[82]A. Zarri, M. B. Botana, J. Christophe, and C. Schram, "Aerodynamic investigation of the turbulent flow past a louvered-fin-and-tube automotive heat exchanger," Exp. Therm. Fluid Sci. **155**, 111182 (2024).

[83]J. L. Lumley and G. R. Newman, "The return to isotropy of homogeneous turbulence," J. Fluid Mech. **82**, 161–178 (1977).

[84]J. L. Lumley, "Computational Modeling of Turbulent Flows," Adv. Appl. Mech. **18**, 123–176 (1978).

[85]K.-S. Choi and J. L. Lumley, "The return to isotropy of homogeneous turbulence," J. Fluid Mech. **436**, 59–84 (2001).

[86]M. Emory and G. Iaccarino, "Visualizing turbulence anisotropy in the spatial domain with componentality contours," Annu. Res. Briefs **2014**, 123–138. https://www.semanticscholar.org/paper/Visualizing-turbulence-anisotropy-in-the-spatial-By-Emory-Iaccarino/5f529ab594acb20bff042e19f6f044b1ae62daba#cited-papers

[87]A. L. Kistler and T. Vrebalovich, "Grid turbulence at large Reynolds numbers," J. Fluid Mech. **26**, 37 (1966).

23 January 2025 12:30:40